

Water films in hydrate-bearing sediments

Hugh Daigle¹ and Alan W Rempel²

¹University of Texas at Austin

²University of Oregon

November 22, 2022

Abstract

At thermodynamic equilibrium, gas hydrates are arranged in the pore space of host sediments to minimize free energy, including the energy of interfaces. Through an analogy with frozen soil, we show that free energy minimization in hydrate-bearing sediments requires the presence of a water film of finite thickness separating hydrate from the sediment grains. The thickness of this premelted layer may be predicted from a balance of intermolecular forces acting across the film. Temperature and porewater salinity are the strongest determiners of premelted layer thickness. We show that, at temperatures and salinities typical of the subsurface or commonly used in laboratory investigations of hydrate-bearing porous media, the premelted layer varies in thickness from microns to sub-nanometer, with thicker layers corresponding to lower salinities and/or higher temperatures. Balance of intermolecular forces predicts that hydrate will be completely nonwetting on hydrophilic surfaces, including silica. We also show that flow through premelted layers may be a significant component of the permeability of hydrate-bearing sediments, particularly at moderate to high hydrate saturation (>60%); and that the electrical conductivity of the premelted layer at needs to be accounted for in assessments of hydrate abundance from subsurface resistivity logs. This work highlights the importance of considering premelted layers when predicting the effects of hydrate on sediment properties.

Water films in hydrate-bearing sediments

Hugh Daigle^{1,2*} and Alan W. Rempel³

¹Center for Subsurface Energy and the Environment, The University of Texas at Austin, Austin, Texas, USA

²Hildebrand Department of Petroleum and Geosystems Engineering, The University of Texas at Austin, Austin, Texas, USA

³Department of Earth Sciences, University of Oregon, Eugene, Oregon, USA

*Corresponding author. Email: daigle@austin.utexas.edu

Key points

- At thermodynamic equilibrium, there is always a thin film of water between gas hydrate and sediment grains
- Film thickness varies from sub-nanometer to microns, with thicker films at warmer temperatures and lower salinities
- Electrical and hydraulic conduction may be significant through the film, especially at moderate to high hydrate saturation (>60%)

Abstract

At thermodynamic equilibrium, gas hydrates are arranged in the pore space of host sediments to minimize free energy, including the energy of interfaces. Through an analogy with frozen soil, we show that free energy minimization in hydrate-bearing sediments requires the presence of a water film of finite thickness separating hydrate from the sediment grains. The thickness of this premelted layer may be predicted from a balance of intermolecular forces acting across the film. Temperature and porewater salinity are the strongest determiners of premelted layer thickness. We show that, at temperatures and salinities typical of the subsurface or commonly used in laboratory investigations of hydrate-bearing porous media, the premelted layer varies in thickness from microns to sub-nanometer, with thicker layers corresponding to lower salinities and/or higher temperatures. Balance of intermolecular forces predicts that hydrate will be completely nonwetting on hydrophilic surfaces, including silica. We also show that flow through premelted layers may be a significant component of the permeability of hydrate-bearing sediments, particularly at moderate to high hydrate saturation (>60%); and that the electrical conductivity of the premelted layer at needs to be accounted for in assessments of hydrate abundance from subsurface resistivity logs. This work highlights the importance of considering premelted layers when predicting the effects of hydrate on sediment properties.

Keywords: gas hydrate, water films, permeability, electrical conductivity

1. Introduction

Recent advances in experimental equipment and methods have allowed an improved understanding of how the presence of gas hydrates affects the properties of their host sediments at in situ conditions [Priest *et al.*, 2015; Santamarina *et al.*, 2015; Yoneda *et al.*, 2017; Boswell *et al.*, 2019; Thomas *et al.*, 2020]. This includes the effects on mechanical strength and fluid flow, which are both important to constrain for energy resource extraction, geohazard assessment, and the role of hydrates in chemical cycling on geologic timescales. One key to this understanding is improving our knowledge of how gas hydrates are distributed within the sediment pore space, that is, whether they form preferentially in pores of a certain size, and whether they assume a pore-filling or grain-coating morphology.

Much of our understanding of the pore-scale distribution of gas hydrates has been informed from analogous work on ice-bearing sediments [e.g., Clennell *et al.*, 1999]. Ice has many parallels to gas hydrates in porous media, including similar thermodynamic behavior and influence on host sediment properties [Lee *et al.*, 2010; Rempel, 2011]. One particularly salient feature of ice in porous media is the tendency of ice not to contact silica grains directly, but rather to coexist with a thin liquid film that wets the grain surfaces and separates them from the ice [Cahn *et al.*, 1992]. The presence and thickness of this premelted layer can be predicted from minimization of total system free energy, while accounting for the free energies of the ice-water and silica-water interfaces, as well as the interactions between ice and silica molecules themselves, modulated by interactions with the molecules in the premelted film that separates them. In this way, premelting can be regarded as a special type of wetting phenomenon in which a solid is wetted by its own melt [e.g., Schick, 1990], with the necessary additional requirement in porous media that the total system free energy remains at a minimum when the pore walls are

wetted by the melt as well. For example, *Hansen-Goos and Wettlaufer* [2010] showed that, over a typical range of temperatures and salinities, the premelted layer between ice and fused quartz is <1-10 nm thick. An analogous premelted layer between gas hydrate and sediment grains could have significant implications for a range of macroscopic sediment properties.

Direct and indirect evidence of such a premelted layer has already been reported in the literature. *Tohidi et al.* [2001] observed a liquid film a few μm thick around the grains in a glass micromodel containing tetrahydrofuran (THF) hydrate and deionized (DI) water. *Chaouachi et al.* [2015] and *Yang et al.* [2016] observed similar μm -scale water films around sand grains in synchrotron images of sand packs containing Xe hydrate and DI water both during hydrate formation and dissociation. Interestingly, *Chaouachi et al.* [2015] also observed that sand grains that had been modified to be hydrophobic tended to be surrounded by a thin layer of Xe gas rather than water, pointing toward the importance of wettability in premelted layer formation. In addition to these image-based observations, measurements of electrical conductivity and acoustic attenuation in hydrate-bearing sediments have indicated the presence of a premelted layer influencing the results. *Spangenberg and Kulenkampff* [2006] compared electrical conductivity measurements of a glass bead pack containing methane hydrate and 100 mM NaCl brine with theoretical models of *Spangenberg* [2001] and found that the observed variation in the resistivity index was best described by a model that included electrical transport through thin liquid films separating the hydrate from the beads. *Priest et al.* [2006] measured compressional and shear wave attenuation in sand packs containing DI water and methane hydrate, and found that the attenuation behavior at low hydrate saturations (<10% of the pore volume) could be described by invoking squirt flow in thin water films separating hydrate from the sand grains. They hypothesized that the phenomenon disappeared at larger hydrate saturations due to a lack of

hydraulic communication between the thin film and neighboring pore bodies as more hydrate filled the pore space.

These observations point to the ubiquitous presence of a premelted layer in hydrophilic porous media, and an influence of that layer on host sediment properties. What is lacking is a framework for predicting the thickness and other properties of the premelted layer. Such a framework is well established both in the frozen soil and petroleum engineering communities [Hirasaki, 1991; Hansen-Goos and Wettlaufer, 2010], and is based on the extended Derjaguin-Landau-Verwey-Overbeek (DLVO) theory of colloidal stability [Derjaguin and Landau, 1941; Verwey and Overbeek, 1948; Berg, 2010], which describes the intermolecular interactions between surfaces at the length scales of interest. We review the existing model for the controls on a premelted layer in frozen soil and apply it to hydrate-bearing sediments to predict premelted layer thickness. We then use the results to predict the wettability of gas hydrate on silica, and the contribution of the premelted layer to fluid flow and electrical conductivity in hydrate-bearing sediments.

2. Thermodynamic equilibrium in water films

2.1 Governing equation

The thermodynamics of thin water films in hydrate-bearing sediments can be understood through analogy with the behavior of premelted ice. Dash *et al.* [2006] and Wettlaufer and Worster [2006] provide excellent reviews on the topic. In porous media, the existence of a premelted layer between hydrate (or ice) and solid mineral grains (Fig. 1) may be explained by minimizing the free energy, which includes contributions both from the bulk aqueous and hydrate phases and the interfaces [Hansen-Goos and Wettlaufer, 2010]. The pressure within the

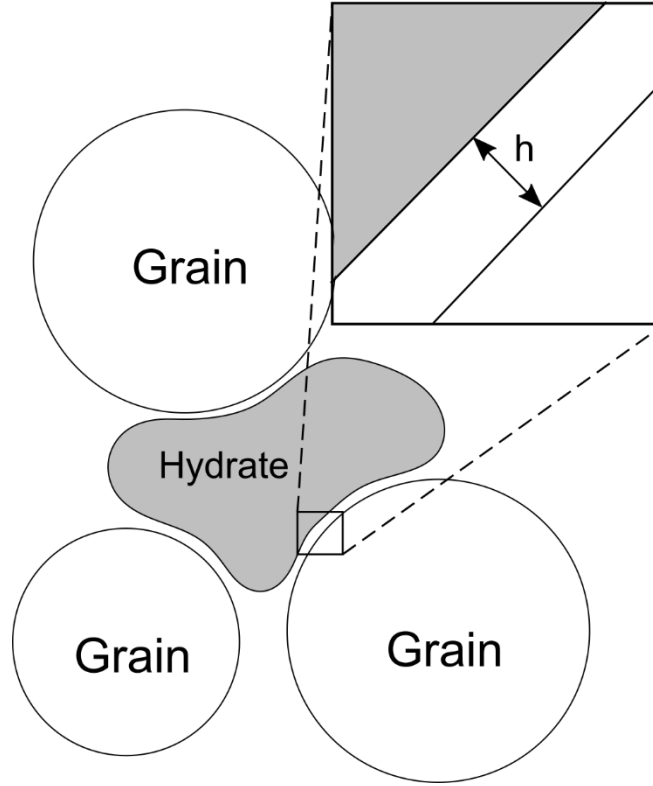


Figure 1. Illustration of a thin water film between hydrate and sediment grains. The film is assumed to be sufficiently thin that its curvature is zero.

premelted layer P_l will be lower than the normal stress on the hydrate interface P_h by an amount equal to the disjoining pressure Π , which represents the force per unit area exerted on the hydrate by the pore walls (a complete list of nomenclature is provided in Table 1). The disjoining pressure can include the effects of various intermolecular forces including van der Waals forces, electrostatic forces, hydrogen bonding, solvation or solvent structuring, steric interactions, and interfacial bending [Berg, 2010]. We consider van der Waals, electrostatic, and solvation interactions since the others are generally much weaker. We also assume that the premelted layer is thin enough that its curvature has a negligible influence on Π . Contributions to the disjoining pressure are additive, so

$$P_h - P_l = \Pi = \Pi_{vdW} + \Pi_e + \Pi_s, \quad (1)$$

where Π_{vdW} , Π_e , and Π_s are the van der Waals, electrostatic, and solvation contributions to Π . If the system is at temperature T and the pressure within the premelted layer is at the bulk melting pressure P_m corresponding to a bulk melting temperature T_m , then Eq. 1 can be combined with the Clausius-Clapeyron equation to yield

$$\rho_h \Delta H \frac{T_m - T}{T_m} = \Pi_{vdW} + \Pi_e + \Pi_s, \quad (2)$$

where ρ_h is the density of solid hydrate and ΔH is the latent heat of fusion [Rempel, 2011]. The difference $T_m - T$ is the undercooling. If impurities like salt are present in the aqueous phase, the colligative effect can be included as an additional term C_T [Hansen-Goos and Wettlaufer, 2010], as can the Gibbs-Thomson effect along an interface with curvature K and hydrate-water interfacial tension σ_{hw} :

$$\rho_h \Delta H \frac{T_m - T}{T_m} = C_T + K \sigma_{hw} + \Pi_{vdW} + \Pi_e + \Pi_s. \quad (3)$$

In this case, T_m is the equilibrium temperature between hydrate and salt-free water along a flat surface that is sufficiently far (i.e., microns) from foreign surfaces that $\Pi \rightarrow 0$. A key feature of hydrate-liquid equilibrium is the presence of dissolved methane in solution, which makes it necessary to specify that the bulk equilibrium temperature in our formulation must be evaluated at the in situ methane concentration.

2.2 Components of the disjoining pressure

Following theory, assuming a film thickness of h (Fig. 1) and treating the hydrate and grain as semi-infinite half-spaces, the van der Waals interaction potential Φ_{vdW} is given by

$$\Phi_{vdW} = -\frac{A_{hg}}{12\pi h^2}, \quad (4)$$

where A_{hg} is the Hamaker constant for hydrate interacting with the grain surface through a water film [Berg, 2010]. Note that Eq. 4 ignores the full frequency dependence of dielectric properties that results in London dispersion and is consequently only the nonretarded contribution. The van der Waals disjoining pressure contribution is obtained as the change in potential with an incremental change in surface separation, so that

$$\Pi_{vdW} = -\frac{\partial \Phi_{vdW}}{\partial h} = -\frac{A_{hg}}{6\pi h^3}. \quad (5)$$

Note that $A_{hg} > 0$ indicates a negative contribution to Π , or an attractive net force, as required for example between identical surfaces immersed in a fluid. Dissimilar surfaces like hydrate and matrix grains that are separated by an aqueous solution with intermediate dielectric properties have $A_{hg} < 0$, thereby causing the two surfaces to repel each other and helping to promote premelting [Wilen *et al.*, 1995].

The electrostatic interaction potential Φ_e is determined by considering the reduction in entropy associated with ordering dissolved ionic species within a premelted layer that separates charged hydrate-water and grain-water surfaces with charge density q_s . In the commonly invoked limit of modest surface potentials,

$$\Phi_e = \frac{2q_s^2}{\kappa\epsilon\epsilon_0} e^{-\kappa h}, \quad (6)$$

where ϵ is the relative dielectric permittivity of the aqueous phase, ϵ_0 is the vacuum dielectric permittivity, N_A is Avogadro's number, I is the ionic strength of the aqueous phase, and κ is the inverse of the Debye length:

$$\kappa = \sqrt{\frac{2e^2 N_A I}{\epsilon\epsilon_0 k_B T}}, \quad (7)$$

where e is the elementary charge and k_B is Boltzmann's constant. Eq. 6 represents the Debye-Hückel limit in which $h \gg \kappa^{-1}$ [Berg, 2010; Hansen-Goos and Wettlaufer, 2010]. The electrostatic disjoining pressure contribution is thus

$$\Pi_e = -\frac{\partial \Phi_e}{\partial h} = \frac{2q_s^2}{\epsilon\epsilon_0} e^{-\kappa h}. \quad (8)$$

We compute ϵ as a function of temperature and salinity using the correlation of Klein and Swift [1977].

At very small h , the forces acting on either side of the layer may no longer be described by continuum models such as the Hamaker or Debye-Hückel approaches for van der Waals and electrostatic forces [Israelachvili, 1987], and the force due to arrangement of individual molecules in the film and Born repulsion opposing overlap of individual molecules must be considered [Berg, 2010]. Detailed measurement of this force, called the solvent structuring or

solvation force since it pertains to solvent molecules (water in the present case), showed that it decays exponentially with h , and that it is oscillatory with a period equal to the diameter of the molecules in the film [Pashley and Israelachvili, 1984; Churaev and Derjaguin, 1985; Christenson, 1986; Derjaguin and Churaev, 1987; Chapel, 1994]. These oscillations are ascribed to the force necessary to squeeze out monolayers of water, with each successive monolayer being more difficult to remove [Israelachvili, 1987; Attard and Parker, 1992; Yaminsky and Christenson, 1995]. Following Derjaguin and Churaev [1987] and Chapel [1994], we represent the solvation disjoining pressure contribution as a double exponential:

$$\Pi_s = K_1 e^{-\frac{h}{h_1}} + K_2 e^{-\frac{h}{h_2}}, \quad (9)$$

where K_1 and K_2 are constants and h_1 and h_2 are decay lengths. Laboratory data necessary to determine these parameters for thin films of water between hydrate (or ice) and silica grains are lacking. However, Chapel [1994] measured the solvation force between sheets of silica in various electrolytes and reported $K_1 = 18.748$ MPa, $h_1 = 0.563$ nm, $K_2 = 20.476$ GPa, and $h_2 = 0.057$ nm for NaCl brine, which we use here. We note here that there is some experimental evidence that increasing ionic strength tends to reduce the magnitude of the solvation force [Derjaguin and Churaev, 1987], though Israelachvili and Adams [1978] and Chapel [1994] specifically report the lack of any such relationship between solvation force and ionic strength. Therefore we neglect the possibility of such an effect.

Combining Eqs. 5, 8, and 9, Eq. 3 can be rewritten in the limit of zero interfacial curvature as

$$\rho_h \Delta H \frac{T_m - T}{T_m} = C_T - \frac{A_{hg}}{6\pi h^3} + \frac{2q_s^2}{\varepsilon \varepsilon_0} e^{-\kappa h} + K_1 e^{-\frac{h}{h_1}} + K_2 e^{-\frac{h}{h_2}}. \quad (11)$$

245

246 The colligative effect C_T can be expressed in different ways. Here, we use the method of
 247 *Bhatnagar et al.* [2007], who considered the change in chemical potential of the aqueous phase
 248 due to the presence of salt by varying the activity of water following *Pitzer and Mayorga* [1973].

249 If we consider the case of a bulk aqueous phase (i.e., $h \rightarrow \infty$) then Eq. 11 becomes

250

$$\rho_h \Delta H \frac{T_m - T}{T_m} = C_T = \rho_h \Delta H \frac{T_m - T_m'}{T_m}, \quad (12)$$

252

253 where T_m' is the bulk equilibrium temperature in the presence of salt. Our final expression for
 254 thermodynamic equilibrium of the premelted layer is

255

$$\rho_h \Delta H \frac{T_m - T}{T_m} = \rho_h \Delta H \frac{T_m - T_m'}{T_m} - \frac{A_{hg}}{6\pi h^3} + \frac{2q_s^2}{\varepsilon \varepsilon_0} e^{-\kappa h} + K_1 e^{-\frac{h}{h_1}} + K_2 e^{-\frac{h}{h_2}}. \quad (13)$$

257

258 Eq. 13 cannot be solved explicitly for h as a function of undercooling and thus requires
 259 implicit solution. This is further complicated by the fact that T appears in the left-hand side, in κ ,
 260 and in ε . To simplify our computations, we use T_m' (the melting temperature with the effect of
 261 salt included) for the temperature when determining κ and ε . Even at extreme values for hydrate-
 262 bearing sediments – $T_m' = 20^\circ\text{C}$ and $T = 3^\circ\text{C}$ with $I = 600$ mM – using T_m' rather than T results
 263 in a 6% error in ε and a 0.3% error in κ . Therefore for natural hydrate systems and laboratory
 264 investigations of hydrate in sediments at relevant conditions this assumption results in only a
 265 small error.

2.3 Interfacial surface charge

The electrostatic term in Eq. 13 assumes that the hydrate-water and grain-water interfaces have the same surface charge density. Although surface charge density can be sensitive to a variety of factors and differing values are certainly possible, given that such differences do not change the essential behavior and that there is no firm evidence to support any particular alternative choice, here we summarize evidence that this assumption is feasible. In aqueous solutions, the formation of an electrical double layer implies that the relevant surface charge for Eq. 13 is that at the outer edge of the Stern layer (the Stern plane), representing the excess surface charge that is not neutralized by the counterions in the Stern layer [Berg, 2010]. The surface charge density should therefore vary with temperature, salinity, and pH. Bolt [1957] reported measurements of the surface charge density of silica in brines of various NaCl concentration at room temperature. At pH = 7, the reported q_s ranged from about -0.01 to -0.05 C/m² at NaCl concentrations from 1 to 1000 mM, with q_s increasing with NaCl concentration. Revil and Glover [1997] calculated the surface charge of silica as a function of pH and salinity at room temperature and arrived at similar results. In hydrate-bearing marine sediments, temperatures typically range from 0°C to about 20°C, representing about a 7% variation in $k_B T$. Since surface charge density scales with $\sqrt{k_B T}$ [Revil and Glover, 1997], q_s in situ in hydrate-bearing these sediments should only differ by <3% from these reported values at the same pH.

Direct measurements of the surface charge density of hydrates are lacking, but it may be estimated from the zeta potential (ζ , the surface potential on the Stern plane). Hydrates, like ice, form an electrical double layer in contact with water and typically have $\zeta < 0$ due to sorption of cations on their exposed hydrogen molecules [Drzymala et al., 1999; Zhang et al., 2008]. The

value of q_s can be obtained from ζ using the Grahame equation [Revil and Glover, 1997; Butt et al., 2003]:

$$q_s = \sqrt{8\epsilon\epsilon_0 k_B T N_A (I + \max[10^{3-\text{pH}}, 10^{3+\text{pH}-\text{pK}_w})] \sinh \frac{e\zeta}{2k_B T}}, \quad (14)$$

where $\text{pK}_w = -\log_{10} K_w$ and K_w is the dissociation constant of water. Salako et al. [2012] reported ζ values for cyclopentane hydrate at 277 K in brines with NaCl concentration up to 10 mM. Taking their measured value of $\zeta = -60$ mV at $I = 10$ mM and assuming $\text{pH} = 7$, Eq. 14 yields $q_s = -0.019$ C/m², which is quite similar to the surface charge density of silica obtained by Bolt [1957] and Revil and Glover [1997] at this salinity after accounting for differences in temperature. We should note here that it has not been demonstrated whether hydrate obeys Eq. 14, though this behavior has been shown with ice [Kallay et al., 2003; Inagawa et al., 2019]. For simplicity therefore we assume that q_s of hydrate is approximately the same as that of silica.

2.4 Film thickness and undercooling

Fig. 2 shows the premelted layer thickness h as a function of undercooling from Eq. 14 for NaCl concentrations of 0.01, 1, 100, and 600 mM using $q_s = -0.01, -0.1$, and -0.5 . These NaCl concentrations were chosen to span the range from typical DI water to seawater. At this pressure, $T_m = 13.26^\circ\text{C}$ using the method of Bhatnagar et al. [2007]. We assumed $\rho_h = 923$ kg/m³ [Helgerud et al., 2009a,b] and $\Delta H = 455.6$ kJ/kg [Gupta et al., 2008]. The Hamaker constant A_{hg} was assumed to be 2.890×10^{-21} J for silica and hydrate separated by a film of water [Bonnefoy et al., 2005]. We note that this value for A_{hg} was calculated a priori. Similar a priori calculations by Wilen et al. [1995] for the Hamaker constant between ice and a substrate separated by a film of

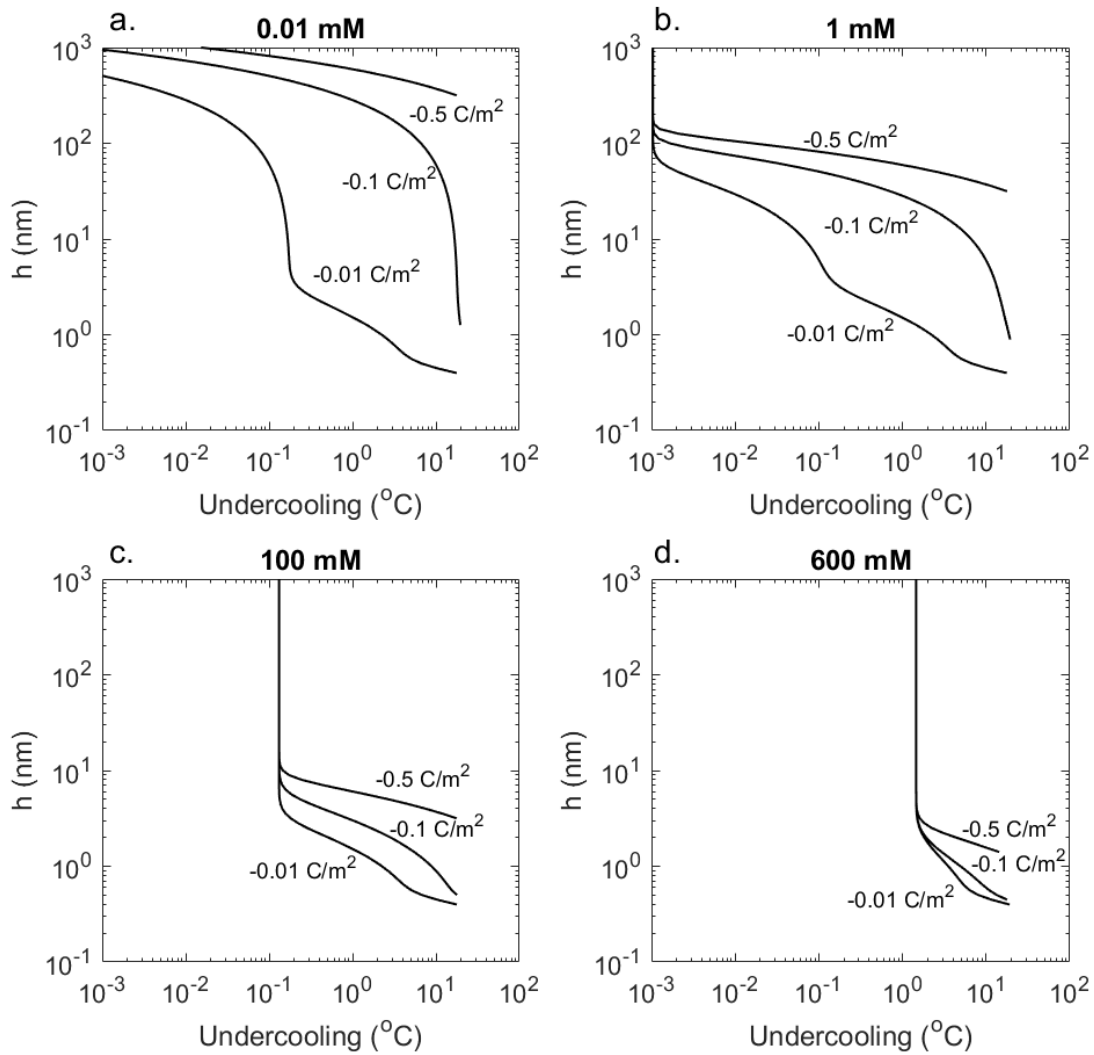


Figure 2. Premelted layer thickness h as a function of undercooling for ionic strengths of 0.01 mM (a), 1 mM (b), 100 mM (c), and 600 mM (d) with surface charge densities of -0.01 , -0.1 , and -0.5 C/m^2 .

water yielded values of $-1.66 \times 10^{-21} \text{ J}$ for silicon and $3 \times 10^{-23} \text{ J}$ for fused silica. On the other hand, *Watanabe and Mizoguchi* [2002] determined a Hamaker constant of $-3.2 \times 10^{-20} \text{ J}$ for ice and glass powder separated by water based on nuclear magnetic resonance measurements of unfrozen water content versus undercooling. The value of A_{hg} we assumed denotes an attractive van der Waals force, in contrast to the solvation and electrostatic forces, which are always

repulsive in our calculations, and based on the comparison to literature values for ice the resulting premelted layer thicknesses should represent minimum estimates. A negative or smaller positive value of A_{hg} would result in less attraction and thus a thicker premelted layer. Calculations were performed to a minimum thickness of 0.275 nm, which is the van der Waals diameter of a water molecule [Zhang and Xu, 1995], or to a maximum undercooling of 20°C.

The data exhibit some common behavior. First, as $T \rightarrow T_m'$ (the melting temperature adjusted for salinity), h approaches infinity. In this situation, Eq. 13 takes the form

$$\frac{A_{hg}}{6\pi h^3} = \frac{2q_s^2}{\epsilon\epsilon_0} e^{-\kappa h} + K_1 e^{-\frac{h}{h_1}} + K_2 e^{-\frac{h}{h_2}}, \quad (15)$$

which is satisfied when $h \rightarrow \infty$. This is consistent with an increasingly thick premelted layer as the melting temperature is approached along with the disappearance of the solid phase at melting, and is consistent with the van der Waals, electrostatic, and solvation interaction potentials tending towards zero at infinite separation [Berg, 2010]. Second, undercooling generally increases as h decreases, and the behavior is dictated by the relative strengths of the interaction potentials. Fig. 3 shows the individual interaction potentials Φ_{vdW} , Φ_e , and Φ_s as well as their sum as a function of h and undercooling for $q_s = -0.1$ C/m² and $I = 0.01$ and 600 mM (recall that the solvation potential $\Phi_s(h) = -\int_h^\infty \Pi_s(h')dh'$). For low salinity ($I = 0.01$ mM), the electrostatic potential is much larger than the van der Waals and solvation potentials, and electrostatic repulsion controls the system behavior. At higher salinities ($I = 600$ mM), the repulsive electrostatic and solvation potentials are similar in magnitude and much larger than the attractive van der Waals potential. None of the conditions we tested results in a net attractive potential, which indicates that a premelted layer will always be present in hydrate-bearing

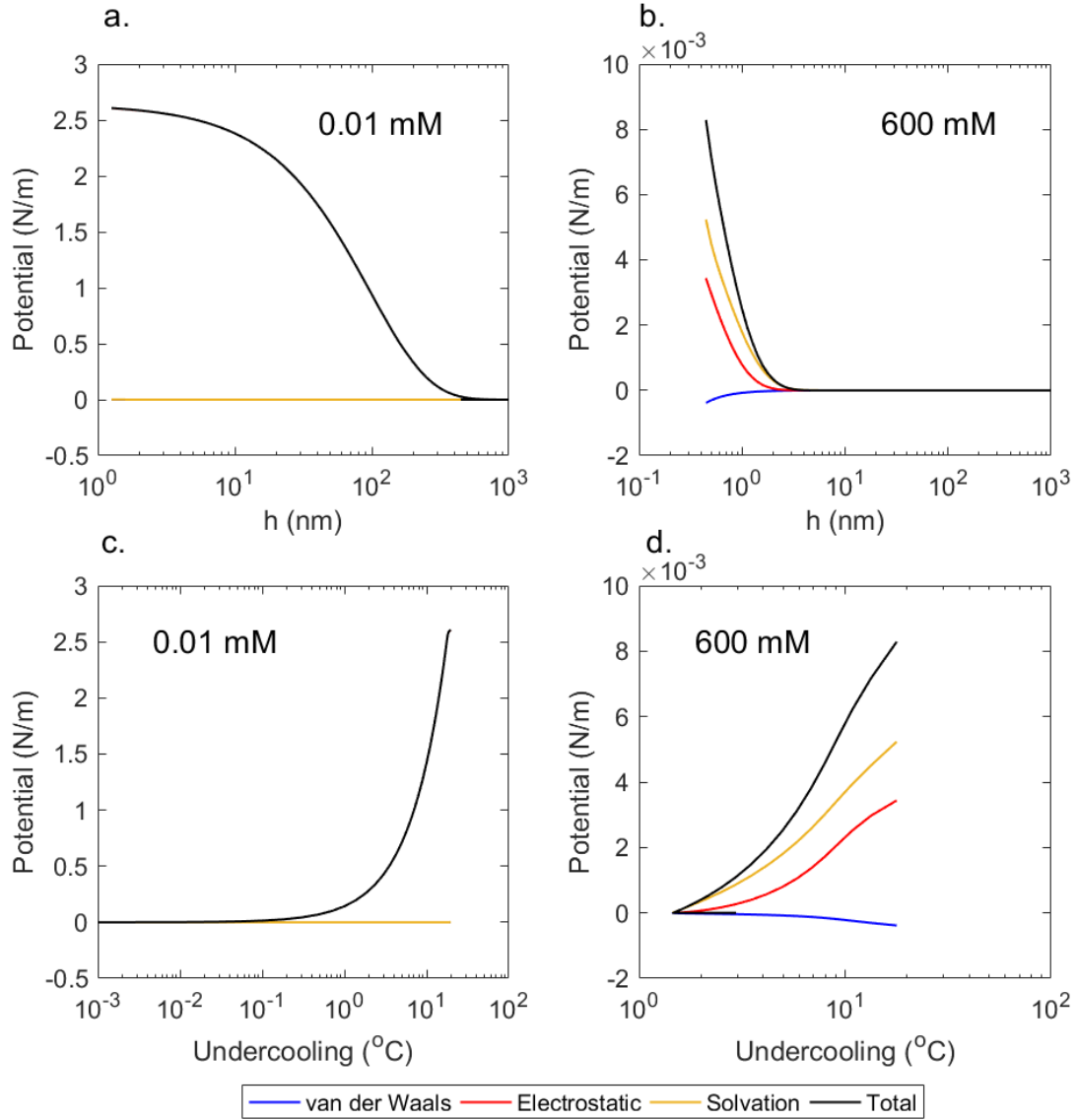


Figure 3. Interaction potentials as a function of premelted layer thickness h for $q_s = -0.1 \text{ C/m}^2$ and ionic strengths of 0.01 mM (a) and 600 mM (b), and as a function of undercooling for ionic strengths of 0.01 mM (c) and 600 mM (d).

sediments. This is mainly due to the assumption that the solvation force does not vary with salinity, since the electrostatic force vanishes for $I > 2300 \text{ mM}$ (corresponding to salinities $> 13.4 \text{ wt\%}$). Detailed investigation of the solvation force under these conditions is warranted since salinities near this value are inferred in the vicinity of gas chimneys from numerical modeling and analysis of field data [Liu and Flemings, 2006; 2007]. The differences in the length scales

over which the potentials act is also noteworthy. At $I = 0.01$ mM, the total potential reaches a value of 0.5 N/m at $h = 160$ nm, while at $I = 600$ mM the total potential is only 0.001 N/m at $h = 1.5$ nm. This is due to the collapse of the electrical double layer at higher salinities, leaving only weak van der Waals attraction and very short-range solvation repulsion as the main interactions. Overall we can conclude that lower salinities will favor thicker premelted layers at a given undercooling.

Our assumption that the influence of the Gibbs-Thomson effect on film thickness can be neglected in Eq. 13 can be assessed here. With $T_m = 13.26^\circ\text{C} = 286.26$ K, the term $\rho_h \Delta H / T_m = 1.5$ MPa/K. Referring back to Fig. 1, approximating the curvature K of the hydrate-water interface as the inverse of the grain radius yields $K\sigma_{hw} = 64$ kPa for grains 1 μm in diameter (assuming $\sigma_{hw} = 0.032$ N/m [Anderson *et al.*, 2003]). The left-hand side of Eq. 13 exceeds this value for undercoolings larger than 0.043°C . For larger grains, $K\sigma_{hw}$ is even smaller and can be neglected even at smaller undercoolings. Smaller grains should consist mainly of platy clay particles with smaller curvature, so the Gibbs-Thomson term can similarly be neglected. We note that the Gibbs-Thomson effect remains important for the residual liquid outside of films near particle contacts where the curved hydrate-liquid interface is sufficiently distant that $\Pi \rightarrow 0$, so that the curvature term in Eq. 3 must be retained. The liquid content in these regions is increasingly important as T_m is approached, however, films dominate the residual liquid volume at the larger undercoolings that accompany higher hydrate saturation levels [e.g., Chen *et al.*, 2020].

3. Implications

3.1 Wettability

It is often assumed that hydrate is nonwetting on silica surfaces through an analogy with ice [Clennell *et al.*, 1999], and laboratory experiments have provided evidence that hydrates are indeed nonwetting in most marine sediments [Daigle, 2016; Murphy *et al.*, 2020]. Wettability has important implications for the distribution of hydrate within the pore space of sediments, capillary effects on hydrate phase equilibrium, and fluid pressures and fluxes during multiphase flow. We parameterize wettability by the contact angle θ , which is the angle subtended by the hydrate-water interface where it contacts a solid substrate as measured through the water (Fig. 4). When a premelted layer is present, the hydrate-water interface does not actually contact the solid substrate, so θ is the contact angle in the limit of zero premelted layer thickness [Hirasaki, 1991]. No contact angle measurements for the hydrate-water interface on silicate minerals are reported in the literature. However, our determination of the disjoining pressure allows us to make some predictions. Here we assume that the shape of the hydrate-water interface can reconfigure itself as needed in the vicinity of a solid surface to minimize free energy. While hydrate is a solid, interfacial reconfiguration through processes like Ostwald or kinetic ripening are well documented in bulk solution and in porous media [Osegovic *et al.*, 2007; Chaouachi *et al.*, 2017; Chen and Espinoza, 2018; Lei *et al.*, 2019], so classical theories that describe wettability in terms of energy minimization will apply here as well [Wettlaufer and Worster, 2006].

From Frumkin-Derjaguin wetting theory [Frumkin, 1938; Derjaguin, 1940], the contact angle is related to the isothermal work required to thin the liquid film from infinite thickness to thickness h :

$$\cos \theta = 1 + \frac{1}{\sigma_{hw}} \left(h\Pi(h) + \int_h^\infty \Pi(h') dh' \right), \quad (16)$$

where σ_{hw} is the hydrate-water interfacial energy [Derjaguin and Churaev, 1987]. If the right-hand side of Eq. 16 is greater than or equal to 1, then $\theta = 0$ [Hirasaki, 1991] and hydrate is completely nonwetting. Fig. 4 shows θ as a function of h for $I = 0.01, 1, 100,$ and 600 mM and $q_s = -0.1 \text{ C/m}^2$ at $P = 10 \text{ MPa}$ and $T_m = 13.26^\circ\text{C}$. We assumed $\sigma_{hw} = 0.032 \text{ N/m}$ [Anderson et al., 2003]. In all cases, θ is generally small ($< 1^\circ$), with higher salinity and q_s closer to zero yielding the larger values. This can be attributed to the reduced repulsive electrostatic forces under these

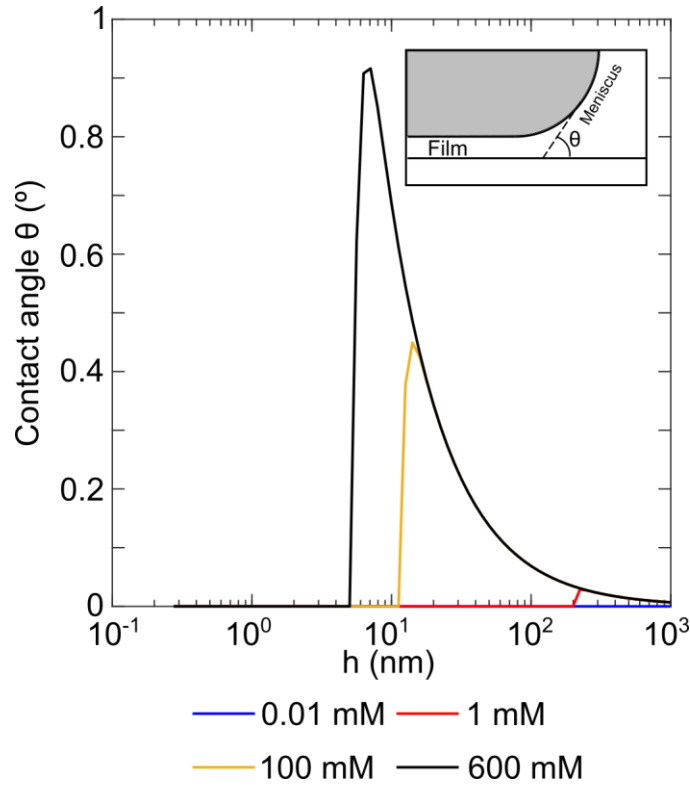


Figure 4. Contact angle θ calculated from Eq. 16 as a function of premelted layer thickness h for different ionic strengths with $q_s = -0.1 \text{ C/m}^2$. Inset illustrates the concept of the macroscopic contact angle θ . Between the film region and the meniscus region, there is a transition region where the hydrate-water interface changes from concave to flat. The macroscopic contact angle is the extrapolation of a line tangent to the meniscus at its innermost limit.

conditions. Similar phenomena have been reported in thin water films between oil droplets and silicate and carbonate minerals, with lower salinities resulting in more hydrophilic behavior [Hirasaki, 1991; Ding and Rahman, 2017]. Therefore we conclude that hydrate is always nonwetting on silica surfaces, and that the assumption that $\theta = 0^\circ$ is valid except in cases of very low surface charge density.

3.2 Fluid flow

The existence of a premelted layer has implications for fluid flow in hydrate-bearing sediments, since water may still move in thin films even at large hydrate saturations when the majority of the pore space is filled with hydrate. Many models have been developed to describe the analogous flow of water in thin films in partially saturated soils [e.g., Toledo *et al.*, 1990; Tuller and Or, 2001; Tokunaga, 2009; Lebeau and Konrad, 2010; Rudiyanto *et al.*, 2015]. As in hydrate-bearing systems, surface energy or capillary effects dominate the liquid content in partially saturated soils above a threshold that depends on the pore size distribution, but thin liquid films become volumetrically more important and act as the dominant hydraulic pathways when the liquid content is diminished. The implied film thicknesses in the soils considered in these models are similar to those we have determined for hydrate-bearing sediments, on the order of a few to 10 nm [Tokunaga, 2009; Lebeau and Konrad, 2010]. However, a significant difference arises in considering the water relative permeability (ratio of unsaturated permeability to saturated permeability), which is the fact that the air-water interface is a free surface while the hydrate-water interface is a solid-liquid interface. These models for unsaturated soils will therefore overpredict water relative permeability due to film flow in hydrate-bearing sediments since the average velocity in the film will be smaller in hydrate-bearing sediments. Models for

frozen soils are more directly analogous. *Lebeau and Konrad* [2012] showed that film flow is the main fluid transport mechanism in fine-grained frozen soils with characteristics similar to marine sediments even at water saturations as large as 0.6, corresponding to undercooling around 0.1 K and premelted layer thicknesses around 10 nm. The relative permeability of the soils under these conditions was on the order of 10^{-4} or smaller, but >4 orders of magnitude larger than the predicted relative permeability using the capillary tube model of *Mualem* [1976] at the same water saturation.

Very little work has been done to investigate the role of fluid transport through films or premelted layers in hydrate-bearing sediments, but an approach similar to that used by *Lebeau and Konrad* [2012] for frozen soil should be valid. One issue that must be considered is the fact that for flow in very thin films, i.e., a few multiples of the mean free path of fluid molecules in the film, continuum descriptions of flow like Darcy's law are not strictly valid and require correction. In particular, the no-slip condition assumed at the solid-fluid interface in continuum flow may not be valid. Noncontinuum flow in a premelted layer of thickness h may be assessed by the Knudsen number Kn , defined as $Kn = \lambda/h$ where λ is the mean free path of the water molecules in the premelted layer. Continuum models are valid for $Kn < 0.01$, but not in the slip flow regime ($0.01 \leq Kn \leq 0.1$) or the transition regime ($Kn > 0.1$). In the slip flow regime, the Navier-Stokes equations can still be used with a correction for nonzero fluid velocity (slip) at the solid-fluid interface following *Maxwell* [1867] who showed that the slip velocity is proportional to the rate of tangential momentum transfer. In the transition regime, intermolecular interactions must be considered more explicitly [*Karniadakis et al.*, 2005]. In the case of diffuse reflection (the tangential velocity of incoming molecules is exactly reversed upon reflection at the solid-

fluid interface), the permeability k for flow of a Newtonian fluid through an infinite slit of aperture h can be corrected for noncontinuum flow as

$$k = \frac{h^2}{2} \left(\frac{1}{6} + \text{Kn} - \text{Kn}^2 \right), \quad (17)$$

which is valid in the slip and transition regimes [Karniadakis *et al.*, 2005]. Eq. 17 may be valid for Kn as high as 1.5 [Sreekanth, 1969]. Fig. 5a shows permeability from Eq. 17 as a function of premelted layer thickness. We determined the mean free path of water following Serway [1990] as $\lambda = V_m / \pi d_w^2 N_A$ where V_m is the molar volume of water and d_w is the diameter of a water molecule. With $V_m = 1.8 \times 10^{-5} \text{ m}^3$ and $d_w = 0.275 \text{ nm}$, we obtained $\lambda = 0.13 \text{ nm}$. The correction for noncontinuum flow is only significant ($>10\%$) for $h < 10 \text{ nm}$, and the permeability decreases from about 10^{-17} m^2 at $h = 10 \text{ nm}$ to about 10^{-20} m^2 at $h = 0.275 \text{ nm}$.

In Figs. 5b and 5c we compare unsaturated or effective permeability as a function of hydrate saturation to the permeability of the premelted layer for several laboratory measurements of water flow in the presence of hydrate. We stress that this is not a true model of relative permeability incorporating film flow, but rather a simple comparison of flow in the pore space and flow in the premelted layer. The lithologies used for these measurements were Berea sandstone [Yousif *et al.*, 1991] and unpreserved sand samples from the Mount Elbert test well on the Alaska North Slope [Johnson *et al.*, 2011]. Premelted layer thickness was determined from experimental pressure and temperature measurements and porewater salinity. Undercooling values were 11.4°C and 6.8°C and the ionic strengths were 260 and 86 mM. This resulted in $h = 0.61 \text{ nm}$ for the Berea sandstone and $h = 1.3 \text{ nm}$ for the Mount Elbert sand. For the Berea sandstone, the permeability of the premelted layer is considerably lower than the measured

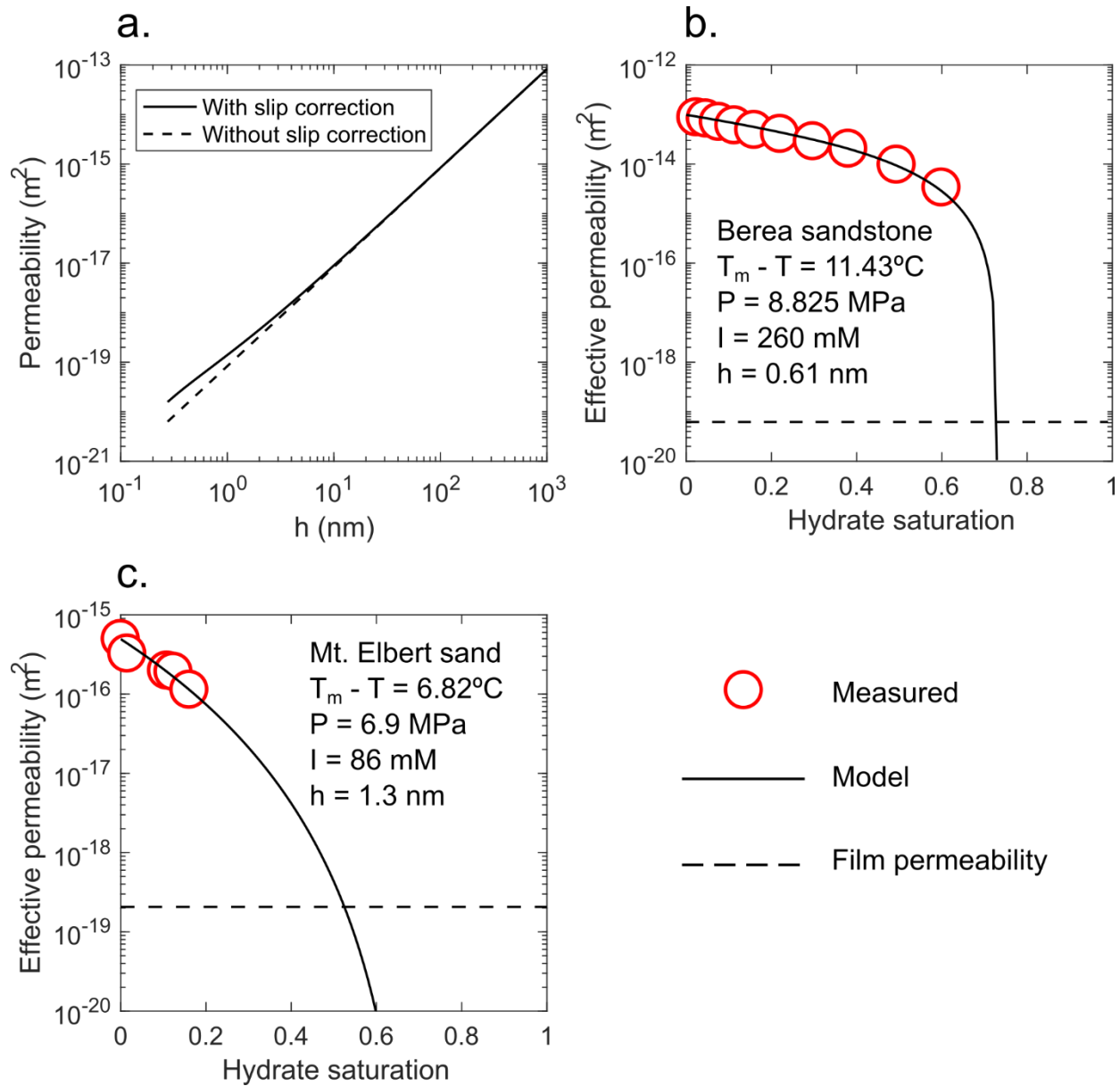


Figure 5. (a) Permeability of an infinite slit-shaped pore with width h from Eq. 17. Dashed line has no slip correction ($Kn = 0$) for comparison. (b) (c) Comparison of laboratory measurements with predicted film permeability from Eq. 17. In all cases, the film thickness (dashed lines) was determined from the reported undercooling and salinity values. Laboratory data sources: Berea sandstone from *Yousif et al.* [1991], Mt. Elbert sand sample from *Johnson et al.* [2011]. Model prediction is from *Daigle* [2016]. Note that the film permeability is not a physically rigorous prediction based on porous medium properties, but simply the permeability of an infinite slit pore with a given aperture.

values until just above the percolation threshold. However, for the Mount Elbert sand sample, the measured effective permeability approaches that of the premelted layer at hydrate saturation around 0.6. This suggests that fluid flow through the premelted layer could be a significant contribution to overall mass transport even at moderate hydrate saturations in samples with intrinsic permeability in the millidarcy ($\sim 10^{-15} \text{ m}^2$) range or lower. The true contribution of film flow is likely larger than we show here since flow will occur over all grain surfaces and not through a single duct [Lebeau and Konrad, 2012].

3.5 Electrical conductivity

Just as the premelted layer can provide an additional pathway for mass transport, so can it provide an electrically conductive path. Here we provide a very simple estimate of the excess conductivity due to the presence of a premelted layer.

In a porous medium containing an electrolyte, electrical conduction occurs both through the bulk electrolyte and the electrical double layer. The electrical conductivities of the bulk fluid and electrical double layer are necessarily different since the ion concentration near a charged surface is altered to maintain electroneutrality and the mobilities of ions in the surface layer are restricted relative to those in bulk solution [Johnson and Sen, 1988; Revil and Glover, 1997]. Surface conduction is mainly due to the ions in the diffuse layer, with the Stern layer contributing a negligible amount [Revil, 2012]. In a thin water film, conduction through the bulk electrolyte will only occur if the film thickness is greater than twice the electrical double layer thickness, or approximately twice the Debye length. Fig. 6 shows the Debye length (κ^{-1}) as a function of ionic strength at $T = 10^\circ\text{C}$ (the difference in κ^{-1} at a given ionic strength over the temperature range $0\text{-}20^\circ\text{C}$ is negligible). Debye length varies from 97 nm at $I = 0.01 \text{ mM}$ to 0.28

nm at $I = 1000$ mM. This means that surface conduction is a more important component of the electrical conductivity at lower salinities, while at higher salinities bulk conduction is more important except at large undercoolings. For example, in seawater ($I = 600$ mM) bulk conduction can only be neglected at undercoolings greater than 7°C (at $q_s = -0.1$ C/m²) based on the corresponding premelted layer thickness. This is overall consistent with the larger Debye length at lower ionic strength.

To provide an estimate of the effect of premelted layer conductivity on the overall conductivity of hydrate-bearing sediments, let us assume a porous medium where the pores consist of parallel cylindrical capillaries with radius of $5\text{ }\mu\text{m}$ (Fig. 7). This pore size is similar to the mode of the pore size distribution observed in the hydrate reservoir at Green Canyon 955 by Fang *et al.* [2020]. This porous medium is obviously too simple to represent real sediments, but

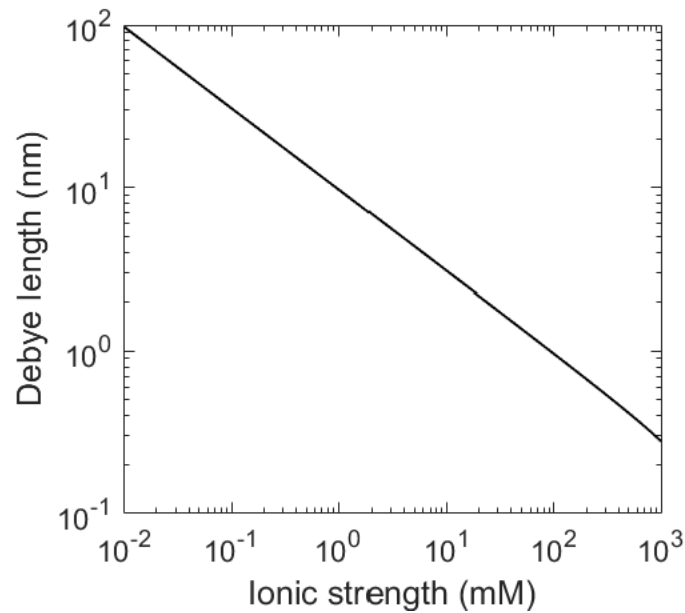


Figure 6. Debye length (κ^{-1}) as a function of ionic strength at $T = 10^\circ\text{C}$.

it will allow us to make some first-order observations. In the absence of hydrate, the direct current (DC) electrical conductivity σ is

$$\sigma = \frac{1}{F} [\sigma_w + (F - 1) \sigma_s], \quad (18)$$

where F is the formation resistivity factor ($= \varphi^{-m}$ where φ is the porosity and m is the cementation exponent), σ_w is the bulk pore fluid conductivity, and σ_s is the surface conductivity [Revil, 2013]. When the pores are straight capillary tubes, $m = 1$ so $F = 1/\varphi$ [Glover, 2009; Revil and Florsch, 2010] and Eq. 18 becomes

$$\sigma = \varphi \left[\sigma_w + \left(\frac{1}{\varphi} - 1 \right) \sigma_s \right]. \quad (19)$$

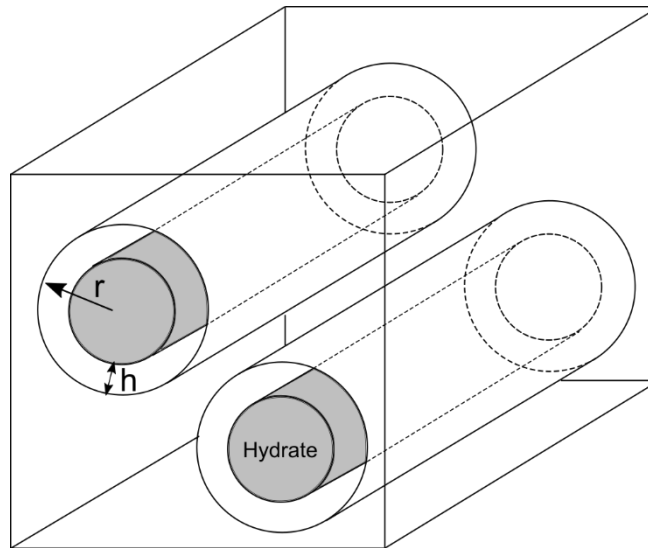


Figure 7. Model porous medium composed of straight, cylindrical pores with pore-filling hydrate. Pore radius and premelted layer are labeled.

In conventional models for the electrical conductivity of partially saturated porous media, surface conduction is assumed only to occur on the solid-liquid interface and not on the gas-water or oil-water interface [e.g., *Waxman and Smits*, 1968; *Revil*, 2013]. In our case, the hydrate-water interface carries a surface charge, so we must consider surface conduction along this interface as well. Assuming that hydrate forms in our cylindrical pores as a concentric cylindrical plug, we can include variable water saturation S_w in Eq. 19 as

$$\sigma = \varphi S_w \left[\sigma_w + \left(\frac{1}{\varphi S_w} - 1 \right) \sigma_s \right], \quad (20)$$

which is only valid for the very simple pore geometry we consider. From inspection of Eq. 20, it can be seen that as $\varphi S_w \rightarrow 0$, $\sigma \rightarrow \sigma_s$. In reality, $\sigma = \sigma_s$ whenever the premelted layer thickness $h \leq 2\kappa^{-1}$. We can correct Eq. 20 for finite electrical double layer thickness by considering the volume occupied by the double layers around the solid matrix and hydrate as (see Appendix A)

$$\sigma = \begin{cases} \varphi \left(1 - S_h - \frac{2(\sqrt{S_h} + 1)}{r\kappa} \right) \left(\sigma_w + \left[\frac{1}{\varphi \left(1 - S_h - \frac{2(\sqrt{S_h} + 1)}{r\kappa} \right)} - 1 \right] \sigma_s \right), & h > 2\kappa^{-1} \\ \sigma_s, & h \leq 2\kappa^{-1} \end{cases}. \quad (21)$$

Note that Eq. 21 neglects the flow of electrical current between the electrical double layer and bulk solution due to ion exchange.

For NaCl solutions σ_w is

$$\sigma_w = e(\beta_+^f + \beta_-^f) N_A I, \quad (22)$$

570

571 where β_+^f and β_-^f are the mobilities of Na^+ cations and Cl^- anions in bulk fluid [Revil and Glover,
572 1997]. Since surface conduction mainly occurs through the diffuse layer, the surface conductivity
573 can be expressed as

574

$$575 \quad \sigma_s = \beta_+^f (1 - f_M) q_s S_s, \quad (23)$$

576

577 where f_M is the fraction of cations in the Stern layer and S_s is the specific surface area of the
578 solids in the medium (surface area per unit volume of solids) [Revil, 2013]. In our model porous
579 medium, solids include matrix and hydrate, and the specific surface area is (see Appendix A)

580

$$581 \quad S_s = \frac{2\varphi(1+\sqrt{S_h})}{r(1-\varphi[1-S_h])}. \quad (24)$$

582

583 For sediments with relatively low $q_s S_s$, i.e., low abundance of clay minerals and low cation
584 exchange capacity, $f_M \approx 0.98$, indicating that almost all cations are contained within the Stern
585 layer [Revil, 2012]. The values of β_+^f and β_-^f are typically given at some reference temperature
586 T_0 , and the conductivities may be adjusted to an arbitrary temperature T as

587

$$588 \quad \sigma_w(T) = (1 + \vartheta_f [T - T_0]) e \left(\beta_+^f(T_0) + \beta_-^f(T_0) \right) N_A I, \quad (25a)$$

589

$$590 \quad \sigma_s(T) = (1 + \vartheta_f [T - T_0]) \beta_+^f(T_0) (1 - f_M) q_s S_s, \quad (25b)$$

591

where $\vartheta_f \approx 0.023 \text{ } ^\circ\text{C}^{-1}$ [Revil *et al.*, 1998]. For Na^+ , $\beta_+^f = 5.19 \times 10^{-8} \text{ m}^2/\text{s}\cdot\text{V}$ at 25°C [Revil *et al.*, 1998] and for Cl^- , $\beta_-^f = 6.5 \times 10^{-8} \text{ m}^2/\text{s}\cdot\text{V}$ at 25°C [Koneshan *et al.*, 1998].

Fig. 8 shows the electrical conductivity from Eq. 21 versus the quantity $\varphi(1 - S_h)$ for $I = 0.01, 1, 100$, and 600 mM with $q_s = -0.1 \text{ C/m}^2$. We assumed a porosity of 40%, which is consistent with shallow, unconsolidated marine sands that might be hydrate reservoirs [Daigle *et al.*, 2015]. Calculations were performed at a constant temperature of 10°C to isolate the effects of premelted layer thickness without considering undercooling. In the absence of surface conductivity, Eq. 21 reduces to Archie's law ($\sigma = \varphi(1 - S_h)\sigma_w$), so a plot of σ versus $\varphi(1 - S_h)$ would yield a straight line with slope σ_w . Deviations from such a line are indications of a contribution from surface conduction, and these lines are included in Fig. 8 for reference. We observe that at low ionic strength, conduction is almost entirely surface-dominated (Fig. 8a). This is due to the thick electrical double layer and low water conductivity. When $I = 0.01$, $2\kappa^{-1} = 194 \text{ nm}$. Since h is related to S_h by $h = r(1 - \sqrt{S_h})$, $h \leq 194 \text{ nm}$ when $S_h \geq 0.92$ or $\varphi(1 - S_h) \leq 0.03$. For $\varphi(1 - S_h) > 0.03$, surface conduction is still a significant part of the overall conduction because $\sigma_s/\sigma_w \approx 0.3$. As I increases, surface conduction becomes less and less important. At $I = 600 \text{ mM}$ (Fig. 8d), $2\kappa^{-1} = 0.75 \text{ nm}$, so bulk fluid conduction stops only at $S_h \geq 0.9997$. The ratio $\sigma_s/\sigma_w \approx 5 \times 10^{-6}$ in this case, indicating an overall negligible contribution to overall conduction.

In Fig. 9, we show the electrical conductivity of our model porous medium as a function of undercooling at $I = 600 \text{ mM}$ and $q_s = -0.1 \text{ C/m}^2$ with the assumption that conduction only occurs through the premelted layer. This plot allows us to make some comparisons with the measured in situ electrical conductivity of some hydrate-bearing sediments with high hydrate saturation ($S_h > 80\%$). The measured conductivities of the four locations we compare range from 0.005 to 0.0125 S/m . For the locations with undercoolings greater than 2°C (the Red Sand at

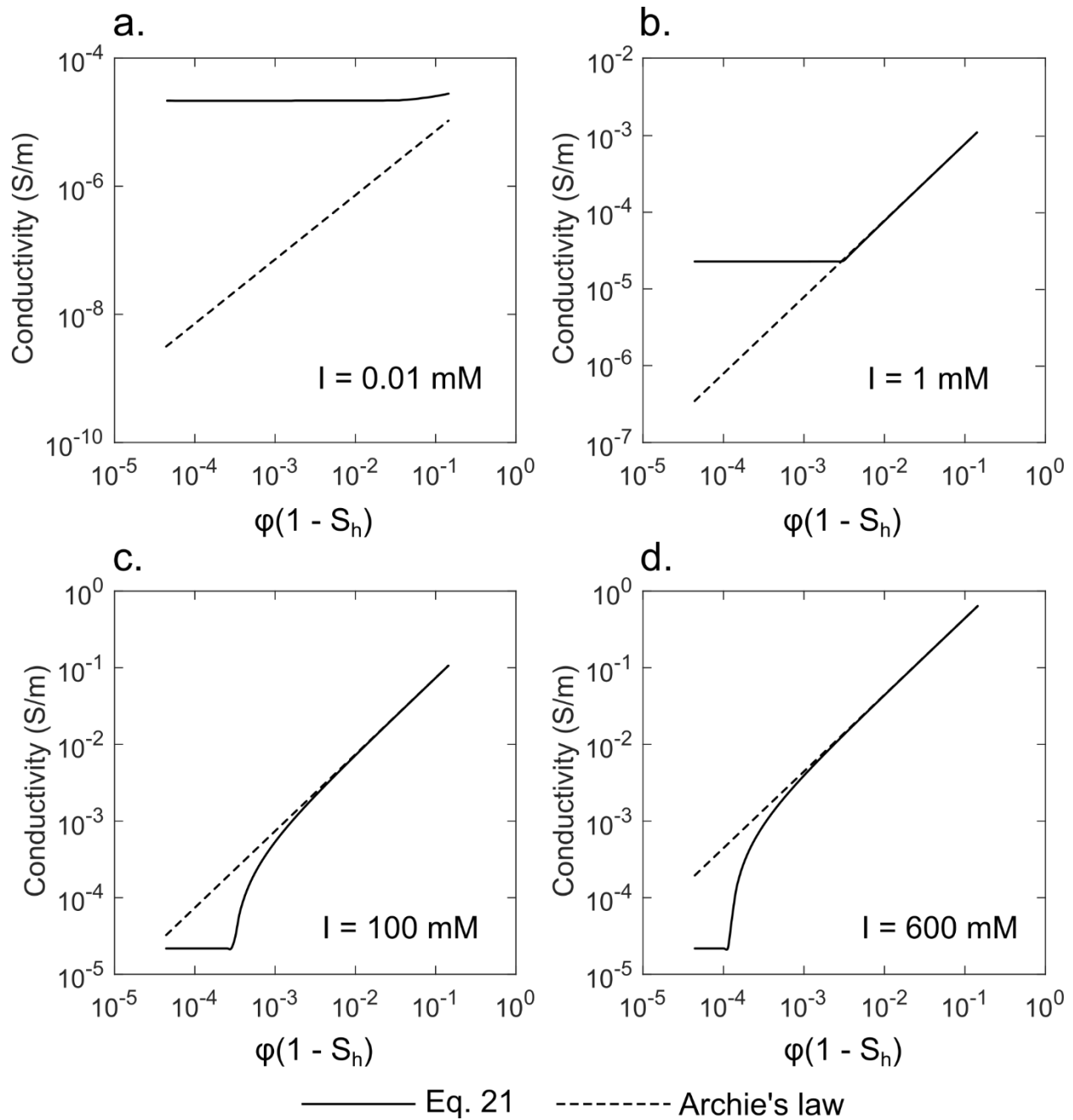


Figure 8. Predicted electrical conductivity at a constant temperature of 10°C for as a function of hydrate saturation in the model porous medium (Fig. 7) at $I = 0.01$ mM (a), 1 mM (b), 100 mM (c), and 600 mM (d). Porosity was fixed constant at 40%. Dashed lines show prediction from Archie's law for comparison, which neglects surface conduction.

Walker Ridge 313H [WR 313H] and the production interval at the AT1 site in the Nankai Trough), the measured conductivities are at least 10 times larger than the predicted conductivity of the premelted layer. For the other two locations (Green Canyon 955 [GC 955] reservoir and the Blue Sand at WR 313H), the measured conductivities approach that of the premelted layer, suggesting that electrical conduction through the premelted layer may be a significant contribution to the overall in situ conductivity of the sediments. This is likely due to a combination of high hydrate saturation, with electrical conductance through the films generally being a more significant component of the overall electrical transport, and the location of these two intervals near the base of the hydrate stability zone, with the corresponding small undercoolings leading to higher film conductivity (assuming that the dissolved methane concentration is equal to the solubility such that the melting temperature corresponds to the

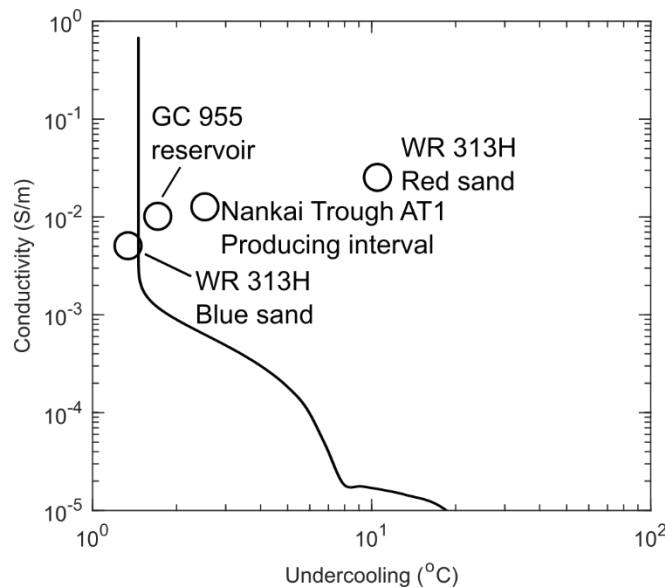


Figure 9. Conductivity of the premelted layer as a function of undercooling for our model porous medium with $I = 600$ mM and $q_s = -0.1$ C/m². Field data from four sand intervals with high hydrate saturation (>80%) are shown as circles for comparison. Data sources: *Fujii et al.* [2015] (Nankai Trough), *McConnell and Kendall* [2002] and *Collett et al.* [2012] (WR 313H), *Collett et al.* [2012] and *Flemings et al.* [2020] (GC 955).

equilibrium temperature at in situ pressure, temperature, and salinity). We do caution that our model porous medium is quite simple, and the true premelted layer conductivity will differ from what we predict.

3.6 Laboratory versus natural systems

One striking result is the difference in film thickness between DI water and seawater. From Fig. 2, at $q_s = -0.1 \text{ C/m}^2$ and 10°C of undercooling, $h = 60 \text{ nm}$ in DI water while $h = 0.6 \text{ nm}$ in seawater – a hundred-fold difference. As we showed, this difference can have significant implications, particularly for fluid flow and mass transport. Indeed, thin films observed directly in images [Tohidi *et al.*, 2001; Chaouachi *et al.*, 2015; Yang *et al.*, 2016] are quite thick, on the order of μm , in part because DI water was used. We note that the interaction potentials in DI water ($I = 0.01 \text{ mM}$) are dominated by electrostatic interactions (Fig. 3) and that premelted layers of micron thickness will be stable at undercoolings of several $^\circ\text{C}$ particularly at larger surface charge densities than considered here. Premelted layers in hydrate-bearing sediments containing brine are significantly thinner than this, which means that any process occurring in situ (fluid flow, Ostwald ripening) will be much slower than what is observed in the laboratory. Careful choice of porewater chemistry is vital for any laboratory work in which transport properties and rates are desired to be compared between the laboratory and the subsurface.

4. Conclusions

As in ice-bearing sediments, hydrate-bearing sediments contain thin premelted layers of water separating the hydrate from the sediment grains. The thickness of this premelted layer may be determined as a function of temperature and salinity from extended DLVO theory by

665 considering van der Waals, electrostatic, and solvation forces. We showed that, for typical
666 temperatures and salinities used in the laboratory and encountered in the subsurface, the
667 premelted layer ranges from sub-nm to hundreds of nm thick, with thicker layers at lower salinity
668 and higher temperature. This is consistent with direct observations of hydrates in micromodels
669 and sand packs.

670 The presence of a premelted layer has significant implications for fluid flow and
671 electrical conductivity, among other properties. Fluid transport and electrical conductivity
672 through the premelted layer are likely important in marine sediments with hydrate saturations
673 >60%, with their influence increasing at lower undercooling (i.e., towards the base of the hydrate
674 stability zone). More rigorous models are necessary to investigate these effects in detail. The
675 effect of the premelted layer must be considered when comparing laboratory results to in situ
676 behavior since the temperatures and salinities used in the laboratory may introduce significant
677 differences in premelted layer thickness.

678 Acknowledgments

680 Support for this work was provided by the University of Texas at Austin. The data on
681 which this article is based are available in *Collett et al.* [2012], *Flemings et al.* [2020], *Fujii et al.*
682 [2015], *Johnson et al.* [2011], *McConnell and Kendall* [2002], and *Yousif et al.* [1991].

683 Appendix A

684 In the simple porous medium shown in Fig. 7, the pores have radius r and length l and
685 each contains a concentric cylinder of hydrate with radius r_h . Since the pores are all the same size
686 and contain the same premelted layer thickness, the hydrate saturation is

688

689
$$S_h = \frac{\pi r_h^2}{\pi r^2} = \left(\frac{r_h}{r}\right)^2, \quad (\text{A1})$$

690

691 and r_h is related to r by

692

693
$$r_h = r\sqrt{S_h}. \quad (\text{A2})$$

694

695 The electrical double layers along the surfaces of the matrix and hydrate have thickness κ^{-1} . In a

696 single pore, the volume of the electrical double layer around the solid matrix $V_{EDL,m}$ is

697

698
$$V_{EDL,m} = \pi r^2 l - \pi \left(r - \frac{1}{\kappa}\right)^2 l = \pi l \left(r^2 - r^2 + \frac{2r}{\kappa} - \frac{1}{\kappa^2}\right) = \pi l \left(\frac{2r}{\kappa} - \frac{1}{\kappa^2}\right), \quad (\text{A3})$$

699

700 and the volume of the electrical double layer around the hydrate $V_{EDL,h}$ is

701

702
$$V_{EDL,h} = \pi \left(r_h + \frac{1}{\kappa}\right)^2 l - \pi r_h^2 l = \pi l \left(r_h^2 + \frac{2r_h}{\kappa} + \frac{1}{\kappa^2} - r_h^2\right) = \pi l \left(\frac{2r_h}{\kappa} + \frac{1}{\kappa^2}\right), \quad (\text{A4})$$

703

704 or

705

706
$$V_{EDL,h} = \pi l \left(\frac{2r\sqrt{S_h}}{\kappa} + \frac{1}{\kappa^2}\right). \quad (\text{A5})$$

707

708 The total volume of both electrical double layers V_{EDL} is

709

$$V_{EDL} = V_{EDL,m} + V_{EDL,h} = \pi l \left(\frac{2r}{\kappa} - \frac{1}{\kappa^2} + \frac{2r\sqrt{S_h}}{\kappa} + \frac{1}{\kappa^2} \right) = \frac{2\pi r l (\sqrt{S_h} + 1)}{\kappa}. \quad (A6)$$

The volume of the pore V_p' that is not occupied by hydrate or contained in either of the electrical double layers is

$$V_p' = \pi r^2 l - \pi r_h^2 l - \frac{2\pi r l (\sqrt{S_h} + 1)}{\kappa} = \pi r^2 l \left(1 - S_h - \frac{2(\sqrt{S_h} + 1)}{r\kappa} \right), \quad (A7)$$

and the ratio of V_p' to the volume of the pore V_p is

$$\frac{V_p'}{V_p} = \frac{\pi r^2 l}{\pi r^2 l} \left(1 - S_h - \frac{2(\sqrt{S_h} + 1)}{r\kappa} \right) = 1 - S_h - \frac{2(\sqrt{S_h} + 1)}{r\kappa}. \quad (A8)$$

The total amount of porosity φ' that is not occupied by hydrate or in an electrical double layer is therefore

$$\varphi' = \varphi \left(1 - S_h - \frac{2(\sqrt{S_h} + 1)}{r\kappa} \right). \quad (A9)$$

Note that this expression becomes $\varphi(1 - S_h)$ or φS_w in the limit of zero electrical double layer thickness (i.e., $\kappa \rightarrow \infty$), which is consistent with Eq. 20. Substituting φ' for φ in Eq. 20 yields Eq. 21.

Calculating the surface conductivity (Eq. 23) requires knowing the specific surface area S_s , which is the ratio of pore surface area to the volume of solid material. In our case, since surface conduction occurs both on the matrix and hydrate surfaces, we must include hydrate in

732 the solid volume. The surface area S in a single pore in our model porous medium with hydrate
 733 saturation S_h is

734

$$735 \quad S = 2\pi r l + 2\pi r_h l = 2\pi r l (1 + \sqrt{S_h}). \quad (\text{A10})$$

736

737 For a volume of porous medium V_T containing n pores, the total surface area is

738

$$739 \quad S = 2n\pi r l (1 + \sqrt{S_h}), \quad (\text{A11})$$

740

741 and the total solid volume V_s is

742

$$743 \quad V_s = V_T - n\pi r^2 l + n\pi r^2 l S_h = V_T - n\pi r^2 l (1 - S_h). \quad (\text{A12})$$

744

745 The specific surface is

746

$$747 \quad S_s = \frac{S}{V_s} = \frac{2n\pi r l (1 + \sqrt{S_h})}{V_T - n\pi r^2 l (1 - S_h)}. \quad (\text{A13})$$

748

749 The porosity is

750

$$751 \quad \varphi = \frac{n\pi r^2 l}{V_T}, \quad (\text{A14})$$

752

753 so

754

$$755 \quad V_T = \frac{n\pi r^2 l}{\varphi}. \quad (\text{A15})$$

756

757 Substituting Eq. A15 into Eq. A13 yields

758

$$759 \quad S_s = \frac{2n\pi r l (1 + \sqrt{S_h})}{\frac{n\pi r^2 l}{\varphi} - n\pi r^2 l (1 - S_h)}, \quad (\text{A16})$$

760

761 and cancelation of terms yields

762

$$763 \quad S_s = \frac{2(1 + \sqrt{S_h})}{\frac{r}{\varphi} - r(1 - S_h)} = \frac{2(1 + \sqrt{S_h})}{r\left[\frac{1}{\varphi} - (1 - S_h)\right]}. \quad (\text{A17})$$

764

765 Multiplying Eq. A17 by φ/φ yields Eq. 24.

766

767

768

769

770

771

772

773

774

775

References

- Anderson, R., Llamedo, M., Tohidi, B., & Burgass, R. W. (2003). Experimental measurement of methane and carbon dioxide clathrate hydrate equilibria in mesoporous silica. *Journal of Physical Chemistry B*, 107(15), 3507-3514. <https://doi.org/10.1021/jp0263370>
- Attard, P., & Parker, J. L. (1992). Oscillatory solvation forces: a comparison of theory and experiment. *Journal of Physical Chemistry*, 96(12), 5086-5093. <https://doi.org/10.1021/j100191a063>
- Berg, J. C. (2010). *An introduction to interfaces & colloids: The bridge to nanoscience*. Hackensack, NJ: World Scientific.
- Bhatnagar, G., Chapman, W. G., Dickens, G. R., Dugan, B., & Hirasaki, G. J. (2007). Generalization of gas hydrate distribution and saturation in marine sediments by scaling of thermodynamic and transport processes. *American Journal of Science*, 307, 861-900. <https://doi.org/10.2475/06.2007.01>
- Bolt, G. H. (1957). Determination of the charge density of silica sols. *Journal of Physical Chemistry*, 61(9), 1166-1169. <https://doi.org/10.1021/j150555a007>
- Bonnefoy, O., Gruy, F., & Herri, J.-M. (2005). Van der Waals interactions in systems involving gas hydrates. *Fluid Phase Equilibria*, 231(2), 176-187. <https://doi.org/10.1016/j.fluid.2005.02.004>
- Boswell, R., Yoneda, J., & Waite, W. F. (2019). India National Gas Hydrate Program Expedition 02 summary of scientific results: Evaluation of natural gas-hydrate-bearing pressure cores. *Marine and Petroleum Geology*, 108, 143-153. <https://doi.org/10.1016/j.marpetgeo.2018.10.020>
- Butt, H.-J., Graf, K., & Kappl, M. (2003). *Physics and chemistry of interfaces*. Weinheim; Wiley-VCH.

799 Cahn, J. W., Dash, J. G., & Fu, H. (1992). Theory of ice premelting in monosized powders.
800 *Journal of Crystal Growth*, 123(1-2), 101-108. [https://doi.org/10.1016/0022-0248\(92\)90014-A](https://doi.org/10.1016/0022-0248(92)90014-A)

801 Chaouachi, M., Falenty, A., Sell, K., Enzmann, F., Kersten, M., Haberthür, D., & Kuhs, W. F.
802 (2015). Microstructural evolution of gas hydrates in sedimentary matrices observed with
803 synchrotron X-ray computed tomographic microscopy. *Geochemistry, Geophysics, Geosystems*,
804 16(6), 1711-1722. <https://doi.org/10.1002/2015GC005811>

805 Chaouachi, M., Neher, S. H., Falenty, A., & Kuhs, W. F. (2017). Time resolved coarsening of
806 clathrate crystals: the case of gas hydrates. *Crystal Growth & Design*, 17(5), 2458-2472.
807 <https://doi.org/10.1021/acs.cgd.6b01875>

808 Chapel, J.-P. (1994). Electrolyte species dependent hydration forces between silica surfaces.
809 *Langmuir*, 10, 4237-4243. <https://doi.org/10.1021/la00023a053>

810 Chen, J., Mei, S., Irizarry, J.T. & Rempel, A.W. (2020). A Monte Carlo approach to
811 approximating the effects of pore geometry on the phase behavior of soil freezing. *Journal of*
812 *Advances in Modeling Earth Systems*, in review.
813 <https://www.essoar.org/doi/pdf/10.1002/essoar.10502494.1>

814 Chen, X., & Espinoza, D. N. (2018). Ostwald ripening changes the pore habit and spatial
815 variability of clathrate hydrate. *Fuel*, 214, 614-622. <https://doi.org/10.1016/j.fuel.2017.11.065>

816 Christenson, H. K. (1986). Interactions between hydrocarbon surfaces in a nonpolar liquid: effect
817 of surface properties on solvation forces. *Journal of Physical Chemistry*, 90(1), 4-6.
818 <https://doi.org/10.1021/j100273a002>

819 Churaev, N. V., & Derjaguin, B. V. (1985). Inclusion of structural forces in the theory of
820 stability of colloids and films. *Journal of Colloid and Interface Science*, 103(2), 542-553.
821 [https://doi.org/10.1016/0021-9797\(85\)90129-8](https://doi.org/10.1016/0021-9797(85)90129-8)

822 Clennell, M. B., Hovland, M., Booth, J. S., Henry, P., & Winters, W. J. (1999). Formation of
 823 natural gas hydrates in marine sediments 1. Conceptual model of gas hydrate growth conditioned
 824 by host sediment properties. *Journal of Geophysical Research*, 104(B10), 22985-23003.
 825 <https://doi.org/10.1029/1999JB900175>

826 Collett, T. S., Lee, M. W., Zyrianova, M. V., Mrozewski, S., Guerin, G., Cook, A. E., &
 827 Goldberg, D. S. (2012). Gulf of Mexico Gas Hydrate Joint Industry Project Leg II logging-while-
 828 drilling data acquisition and analysis. *Marine and Petroleum Geology*, 34(1), 41-61.
 829 <https://doi.org/10.1016/j.marpetgeo.2011.08.003>

830 Daigle, H. (2016). Relative permeability to water or gas in the presence of hydrates in porous
 831 media from critical path analysis. *Journal of Petroleum Science and Engineering*, 146, 526-535.
 832 <https://doi.org/10.1016/j.petrol.2016.07.011>

833 Daigle, H., Cook, A., & Malinverno, A. (2015). Permeability and porosity of hydrate-bearing
 834 sediments in the northern Gulf of Mexico. *Marine and Petroleum Geology*, 68(A), 551-564.
 835 <https://doi.org/10.1016/j.marpetgeo.2015.10.004>

836 Dash, J. G., Rempel, A. W., & Wettlaufer, J. S. (2006). The physics of premelted ice and its
 837 geophysical consequences. *Reviews of Modern Physics*, 78, 695-741.
 838 <https://doi.org/10.1103/RevModPhys.78.695>

839 Derjaguin, B. V. (1940). Theory of capillary condensation and other capillary phenomena
 840 accounting for the disjoining pressure of polymolecular liquid films. *Acta Physicochimica URSS*,
 841 12, 181-200.

842 Derjaguin, B. V., & Churaev, N. V. (1987). Structure of water in thin layers. *Langmuir*, 3(5),
 843 607-612. <https://doi.org/10.1021/la00077a002>

844 Derjaguin, B. V., & Landau, L. (1941). Theory of the stability of strongly charged lyophobic sols
845 and of the adhesion of strongly charged particles in solutions of electrolytes. *Acta*
846 *Physicochimica URSS*, 14, 633-662.

847 Ding, H., & Rahman, S. (2017). Experimental and theoretical study of wettability alteration
848 during low salinity water flooding – a state of the art review. *Colloids and Surfaces A:*
849 *Physicochemical and Engineering Aspects*, 520, 622-639.
850 <https://doi.org/10.1016/j.colsurfa.2017.02.006>

851 Drzymala, J., Sadowski, Z., Holysz, L., & Chibowski, E. (1999). Ice/water interface: zeta
852 potential, point of zero charge, and hydrophobicity. *Journal of Colloid and Interface Science*,
853 220(2), 229-234. <https://doi.org/10.1006/jcis.1999.6528>

854 Fang, Y., Flemings, P. B., Daigle, H., Phillips, S. C., Meazell, P. K., & You, K. (2020).
855 Petrophysical properties of the GC 955 hydrate reservoir inferred from reconstituted sediments:
856 Implications for hydrate formation and production. *AAPG Bulletin*.
857 <https://doi.org/10.1306/01062019165>

858 Flemings, P. B., Phillips, S. C., Boswell, R., Collett, T. S., Cook, A. E., Dong, T., et al. (2020).
859 Pressure coring a Gulf of Mexico deepwater turbidite gas hydrate reservoir: Initial results from
860 the UT-GOM2-1 Hydrate Pressure Coring Expedition. *AAPG Bulletin*.
861 <https://doi.org/10.1306/05212019052>

862 Frumkin, A. (1938). Phenomena of wetting and the adhesion of bubbles. *Zhurnal Fizicheskoi*
863 *Khimii*, 12, 337-345.

864 Fujii, T., Suzuki, K., Takayama, T., Tamaki, M., Komatsu, Y., Konno, Y., et al. (2015).
865 Geological setting and characterization of a methane hydrate reservoir distributed at the first
866 offshore production test site on the Daini-Atsumi Knoll in the eastern Nankai Trough, Japan.

867 *Marine and Petroleum Geology*, 66(2), 310-322.

868 <https://doi.org/10.1016/j.marpetgeo.2015.02.037>

869 Glover, P. (2009). What is the cementation exponent? A new interpretation. *The Leading Edge*,

870 28(1), 82-85. <https://doi.org/10.1190/1.3064150>

871 Gupta, A., Lachance, J., Sloan, E. D., & Koh, C. A. (2008). Measurements of methane hydrate

872 heat of dissociation using high pressure differential scanning calorimetry. *Chemical Engineering*

873 *Science*, 63(24), 5848-5853. <https://doi.org/10.1016/j.ces.2008.09.002>

874 Hansen-Goos, H., & Wettlaufer, J. S. (2010). Theory of ice premelting in porous media. *Physical*

875 *Review E*, 81(3), 031604. <https://doi.org/10.1103/PhysRevE.81.031604>

876 Helgerud, M. B., Waite, W. F., Kirby, S. H., & Nur, A. (2009a). Elastic wave speeds and moduli

877 in polycrystalline ice Ih, sI methane hydrate, and sII methane-ethane hydrate. *Journal of*

878 *Geophysical Research Solid Earth*, 114(B2), B02212. <https://doi.org/10.1029/2008JB006132>

879 Helgerud, M. B., Waite, W. F., Kirby, S. H., & Nur, A. (2009b). Correction to “Elastic wave

880 speeds and moduli in polycrystalline ice Ih, sI methane hydrate, and sII methane-ethane

881 hydrate”. *Journal of Geophysical Research Solid Earth*, 114(B4), B04299.

882 <https://doi.org/10.1029/2009JB006451>

883 Hirasaki, G. J. (1991). Wettability: fundamentals and surface forces. *SPE Formation Evaluation*,

884 6(2), 217-226. <https://doi.org/10.2118/17367-PA>

885 Inagawa, A., Harada, M., & Okada, T. (2019). Charging of the ice/solution interface by

886 deprotonation of dangling bonds, ion adsorption, and ion uptake in an ice crystal as revealed by

887 zeta potential determination. *The Journal of Physical Chemistry C*, 123(10), 6062-6069.

888 <https://doi.org/10.1021/acs.jpcc.8b12435>

889 Israelachvili, J. (1987). Solvation forces and liquid structure, as probed by direct force
 890 measurements. *Accounts of Chemical Research*, 20(11), 415-421.
 891 <https://doi.org/10.1021/ar00143a005>

892 Israelachvili, J., & Adams, G. E. (1978). Measurement of forces between two mica surfaces in
 893 aqueous electrolyte solutions in the range 0-100 nm. *Journal of the Chemical Society, Faraday*
 894 *Transactions 1*, 74, 975-1001. <https://doi.org/10.1039/F19787400975>

895 Johnson, A., Patil, S., & Dandekar, A. (2011). Experimental investigation of gas-water relative
 896 permeability for gas-hydrate-bearing sediments from the Mount Elbert Gas Hydrate Stratigraphic
 897 Test Well, Alaska North Slope. *Marine and Petroleum Geology*, 28(2), 419-426.
 898 <https://doi.org/10.1016/j.marpetgeo.2009.10.013>

899 Johnson, D. L., & Sen, P. N. (1988). Dependence of the conductivity of a porous medium on
 900 electrolyte conductivity. *Physical Review B*, 37(7), 3502-3510.
 901 <https://doi.org/10.1103/PhysRevB.37.3502>

902 Kallay, N., Čop, A., Chibowski, E., & Holysz, L. (2003). Reversible charging of the ice-water
 903 interface II. Estimation of equilibrium parameters. *Journal of Colloid and Interface Science*, 259,
 904 89-96. [https://doi.org/10.1016/S0021-9797\(02\)00179-0](https://doi.org/10.1016/S0021-9797(02)00179-0)

905 Karniadakis, G., Beskok, A., & Aluru, N. (2005). *Microflows and nanoflows: Fundamentals and*
 906 *simulation*. New York, NY: Springer.

907 Klein, L., & Swift, C. (1977). An improved model for the dielectric constant of sea water at
 908 microwave frequencies. *IEEE Transactions on Antennas and Propagation*, 25(1), 104-111.
 909 <https://doi.org/10.1109/TAP.1977.1141539>

910 Koneshan, S., Rasaiah, J. C., Lynden-Bell, R. M., & Lee, S. H. (1998). Solvent structure,
 911 dynamics, and ion mobility in aqueous solutions at 25°C. *The Journal of Physical Chemistry B*,
 912 102, 4193-4204. <https://doi.org/10.1021/jp980642x>

913 Lebeau, M., & Konrad, J.-M. (2010). A new capillary and thin film flow model for predicting the
 914 hydraulic conductivity of unsaturated porous media. *Water Resources Research*, 46(12),
 915 W12554. <https://doi.org/10.1029/2010WR009092>

916 Lebeau, M., & Konrad, J.-M. (2012). An extension of the capillary and thin film flow model for
 917 predicting the hydraulic conductivity of air-free frozen porous media. *Water Resources*
 918 *Research*, 48(7), W07523. <https://doi.org/10.1029/2012WR011916>

919 Lee, J. Y., Santamarina, J. C., & Ruppel, C. (2010). Volume change associated with formation
 920 and dissociation of hydrate in sediment. *Geochemistry, Geophysics, Geosystems*, 11(3), Q03007.
 921 <https://doi.org/10.1029/2009GC002667>

922 Lei, L., Seol, Y., Choi, J.-H., & Kneafsey, T. J. (2019). Pore habit of methane hydrate and its
 923 evolution in sediment matrix – Laboratory visualization with phase-contrast micro-CT. *Marine*
 924 *and Petroleum Geology*, 104, 451-467. <https://doi.org/10.1016/j.marpetgeo.2019.04.004>

925 Liu, X., & Flemings, P. B. (2006). Passing gas through the hydrate stability zone at southern
 926 Hydrate Ridge, offshore Oregon. *Earth and Planetary Science Letters*, 241, 211-226.
 927 <https://doi.org/10.1016/j.epsl.2005.10.026>

928 Liu, X., & Flemings, P. B. (2007). Dynamic multiphase flow model of hydrate formation in
 929 marine sediments. *Journal of Geophysical Research Solid Earth*, 112(B3), B03101.
 930 <https://doi.org/10.1029/2005JB004227>

931 Maxwell, J. C. (1867). On the dynamical theory of gases. *Philosophical Transactions of the*
 932 *Royal Society*, 157, 49-88. <https://doi.org/10.1098/rstl.1867.0004>

933 McConnell, D. R., & Kendall, B. A. (2002). *Images of the base of gas hydrate stability,*
934 *northwest Walker Ridge, Gulf of Mexico.* Paper presented at Offshore Technology Conference,
935 Offshore Technology Conference, Houston, TX.

936 Mualem, Y. (1976). A new model for predicting the hydraulic conductivity of unsaturated porous
937 media. *Water Resources Research*, 12(3), 513-522. <https://doi.org/10.1029/WR012i003p00513>

938 Murphy, Z. W., DiCarlo, D. A., Flemings, P. B., & Daigle, H. (2020). Hydrate is a non-wetting
939 phase in porous media. *Geophysical Research Letters*. <https://doi.org/10.1029/2020GL089289>

940 Osegovic, J. P., Tatro, S. R., Holman, S. A., Ames, A. L., & Max, M. D. (2007). Growth kinetics
941 of ethane hydrate from a seawater solution at an ethane gas interface. *Journal of Petroleum*
942 *Science and Engineering*, 56(1-3), 42-46. <https://doi.org/10.1016/j.petrol.2005.08.003>

943 Pashley, R. M., & Israelachvili, J. N. (1984). Molecular layering of water in thin films between
944 mica surfaces and its relation to hydration forces. *Journal of Colloid and Interface Science*,
945 101(2), 511-523. [https://doi.org/10.1016/0021-9797\(84\)90063-8](https://doi.org/10.1016/0021-9797(84)90063-8)

946 Pitzer, J. S., & Mayorga, G. (1973). Thermodynamics of electrolytes. II. Activity and osmotic
947 coefficients for strong electrolytes with one or both ions univalent. *Journal of Physical*
948 *Chemistry*, 77(19), 2300-2308. <https://doi.org/10.1021/j100638a009>

949 Priest, J. A., Best, A. I., & Clayton, C. R. I. (2006). Attenuation of seismic waves in methane gas
950 hydrate-bearing sand. *Geophysical Journal International*, 164(1), 149-159.
951 <https://doi.org/10.1111/j.1365-246X.2005.02831.x>

952 Priest, J. A., Druce, M., Roberts, J., Schultheiss, P., Nakatsuka, Y., & Suzuki, K. (2015). PCATS
953 Triaxial: A new geotechnical apparatus for characterizing pressure cores from the Nankai
954 Trough, Japan. *Marine and Petroleum Geology*, 66(2), 460-470.
955 <https://doi.org/10.1016/j.marpetgeo.2014.12.005>

956 Rempel, A. W. (2011). A model for the diffusive growth of hydrate saturation anomalies in
 957 layered sediments. *Journal of Geophysical Research Solid Earth*, 116(B10), B10105.
 958 <https://doi.org/10.1029/2011JB008484>

959 Revil, A. (2012). Spectral induced polarization of shaly sands: Influence of the electrical double
 960 layer. *Water Resources Research*, 48(2), W02517. <https://doi.org/10.1029/2011WR011260>

961 Revil, A. (2013). Effective conductivity and permittivity of unsaturated porous materials in the
 962 frequency range 1 mHz – 1 GHz. *Water Resources Research*, 49(1), 306-327.
 963 <https://doi.org/10.1029/2012WR012700>

964 Revil, A., & Florsch, N. (2010). Determination of permeability from spectral induced
 965 polarization in granular media. *Geophysical Journal International*, 181, 1480-1498.
 966 <https://doi.org/10.1111/j.1365-246X.2010.04573.x>

967 Revil, A., & Glover, P. W. J. (1997). Theory of ionic-surface electrical conduction in porous
 968 media. *Physical Review B*, 55(3), 1757-1773. <https://doi.org/10.1103/PhysRevB.55.1757>

969 Revil, A., Cathles, L. M., Losh, S., & Nunn, J. A. (1998). Electrical conductivity in shaly sands
 970 with geophysical implications. *Journal of Geophysical Research Solid Earth*, 103(B10), 23925-
 971 23936. <https://doi.org/10.1029/98JB02125>

972 Rudiyanto, Sakai, M., van Genuchten, M. T., Alazba, A. A., Setiawan, B. I., & Minasny, B.
 973 (2015). A complete soil hydraulic model accounting for capillary and adsorptive water retention,
 974 capillary and film conductivity, and hysteresis. *Water Resources Research*, 51, 8757-8772.
 975 <https://doi.org/10.1002/2015WR017703>

976 Salako, O., Lo, C., Zhang, J. S., Couzis, A., Somasundaran, P., & Lee, J. W. (2012). Adsorption
 977 of sodium dodecyl sulfate onto clathrate hydrates in the presence of salt. *Journal of Colloid and*
 978 *Interface Science*, 386(1), 333-337. <https://doi.org/10.1016/j.jcis.2012.07.017>

979 Santamarina, J. C., Dai, S., Terzariol, M., Jang, J., Waite, W. F., Winters, W. J., et al. (2015).
 980 Hydro-bio-geomechanical properties of hydrate-bearing sediments from Nankai Trough. *Marine*
 981 *and Petroleum Geology*, 66(2), 434-450. <https://doi.org/10.1016/j.marpetgeo.2015.02.033>
 982 Schick, M. (1990). Introduction to wetting phenomena. In J. Charvolin, J. F. Joanny, and J. Zinn-
 983 Justin (Eds.), *Liquids at interfaces*, Les Houches Lectures Session XLVIII (pp. 415-497).
 984 Amsterdam: Elsevier.
 985 Serway, R. (1990). *Physics for scientists and engineers with modern physics* (3rd ed.).
 986 Philadelphia, PA: Saunders College Publishing.
 987 Spangenberg, E. (2001). Modeling of the influence of gas hydrate content on the electrical
 988 properties of porous sediments. *Journal of Geophysical Research Solid Earth*, 106(B4), 6535-
 989 6548. <https://doi.org/10.1029/2000JB900434>
 990 Spangenberg, E., & Kulenkampff, J. (2006). Influence of methane hydrate content on electrical
 991 sediment properties. *Geophysical Research Letters*, 33(2), L24315.
 992 <https://doi.org/10.1029/2006GL028188>
 993 Sreekanth, A. K. (1969). Slip flow through long circular tubes. In L. Trilling and H. Wachman
 994 (Eds.), *Proceedings of the sixth international symposium on rarefied gas dynamics* (Vol. 1, pp.
 995 667-680). New York, NY: Academic Press.
 996 Thomas, C., Phillips, S. C., Flemings, P. B., Santra, M., Hammon, H., Collett, T. S., et al.
 997 (2020). Pressure coring operations during Expedition UT-GOM2-1 in Green Canyon Block 955,
 998 northern Gulf of Mexico. *AAPG Bulletin*. <https://doi.org/10.1306/02262019036>
 999 Tohidi, B., Anderson, R., Clennell, M. B., Burgass, R. W., & Biderkab, A. B. (2001). Visual
 1000 observation of gas-hydrate formation and dissociation in synthetic porous media by means of

1001 glass micromodels. *Geology*, 29(9), 867-870. [https://doi.org/10.1130/0091-](https://doi.org/10.1130/0091-7613(2001)029%3C0867:VOOGHF%3E2.0.CO;2)
 1002 [7613\(2001\)029%3C0867:VOOGHF%3E2.0.CO;2](https://doi.org/10.1130/0091-7613(2001)029%3C0867:VOOGHF%3E2.0.CO;2)
 1003 Tokunaga, T. K. (2009). Hydraulic properties of adsorbed water films in unsaturated porous
 1004 media. *Water Resources Research*, 45(6), W06415. <https://doi.org/10.1029/2009WR007734>
 1005 Toledo, P. G., Novy, R. A., Davis, H. T., & Scriven, L. E. (1990). Hydraulic conductivity of
 1006 porous media at low water content. *Soil Science Society of America Journal*, 54(3), 673-679.
 1007 <https://doi.org/10.2136/sssaj1990.03615995005400030007x>
 1008 Tuller, M., & Or, D. (2001). Hydraulic conductivity of variably saturated porous media: Film
 1009 and corner flow in angular pore space. *Water Resources Research*, 37(5), 1257-1276.
 1010 <https://doi.org/10.1029/2000WR900328>
 1011 Verwey, E. J. W., & Overbeek, J. T. G. (1948). *Theory of the stability of lyophobic colloids*.
 1012 Amsterdam: Elsevier.
 1013 Watanabe, K., & Mizoguchi, M. (2002). Amount of unfrozen water in frozen porous media
 1014 saturated with solution. *Cold Regions Science and Technology*, 34(2), 103-110.
 1015 [https://doi.org/10.1016/S0165-232X\(01\)00063-5](https://doi.org/10.1016/S0165-232X(01)00063-5)
 1016 Waxman, M. H., & Smits, L. J. M. (1968). Electrical conductivities in oil-bearing shaly sands.
 1017 *SPE Journal*, 8(2), 107-122. <https://doi.org/10.2118/1863-A>
 1018 Wettlaufer, J. S., & Worster, M. G. (2006). Premelting dynamics. *Annual Review of Fluid*
 1019 *Mechanics*, 38, 427-452. <https://doi.org/10.1146/annurev.fluid.37.061903.175758>
 1020 Wilen, L. A., Wettlaufer, J. S., Elbaum, M., & Schick, M. (1995). Dispersion-force effects in
 1021 interfacial premelting of ice. *Physical Review B*, 52(16), 12426-12433.
 1022 <https://doi.org/10.1103/PhysRevB.52.12426>

1023 Yaminsky, V. V., & Christenson, H. K. (1995). Thermodynamic analysis of solute effects on
 1024 oscillatory solvation forces. *Journal of Physical Chemistry*, 99(14), 5176-5179.
 1025 <https://doi.org/10.1021/j100014a044>

1026 Yang, L., Falenty, A., Chaouachi, M., Haberthür, D., & Kuhs, W. F. (2016). Synchrotron X-ray
 1027 computed microtomography study on gas hydrate decomposition in a sedimentary matrix.
 1028 *Geochemistry, Geophysics, Geosystems*, 17(9), 3717-3732.
 1029 <https://doi.org/10.1002/2016GC006521>

1030 Yoneda, J., Masui, A., Konno, Y., Jin, Y., Kida, M., Katagiri, J., et al. (2017). Pressure-core-
 1031 based reservoir characterization for geomechanics: Insights from gas hydrate drilling during
 1032 2012–2013 at the eastern Nankai Trough. *Marine and Petroleum Geology*, 86, 1-16.
 1033 <https://doi.org/10.1016/j.marpetgeo.2017.05.024>

1034 Yousif, M. H., Abass, H. H., Selim, M. S., & Sloan, E. D. (1991). Experimental and theoretical
 1035 investigation of methane-gas-hydrate dissociation in porous media. *SPE Reservoir Engineering*,
 1036 6(1), 69-76. <https://doi.org/10.2118/18320-PA>

1037 Zhang, J. S., Lo, C., Somasundaran, P., Lu, S., Couzis, A., & Lee, J. W. (2008). Adsorption of
 1038 sodium dodecyl sulfate at THF hydrate/liquid interface. *Journal of Physical Chemistry C*,
 1039 112(32), 12381-12385. <https://doi.org/10.1021/jp801963c>

1040 Zhang, Y., & Xu, Z. (1995). Atomic radii of noble gas elements in condensed phases. *American*
 1041 *Mineralogist*, 80(7-8), 670-675. <https://doi.org/10.2138/am-1995-7-803>

1042

Symbol	Description	Dimensions
A_{hg}	Hamaker constant for hydrate-grain interaction	ML^2/T^2
C_T	Colligative contribution to film pressure	M/LT^2
d_w	Water molecular diameter	L

e	Elementary charge	$M^{1/2}L^{3/2}/T$
F	Formation resistivity factor	L^3/L^3
f_M	Fraction of cations in Stern layer	-
h	Premelted layer thickness	L
h_1, h_2	Solvation pressure decay lengths	L
I	Ionic strength	mol/L^3
K	Curvature of hydrate-water interface	$1/L$
K_1, K_2	Solvation pressure constants	M/LT^2
k_B	Boltzmann's constant	$ML^2/T^2\theta$
Kn	Knudsen number	L/L
K_w	Dissociation constant of water	-
l	Pore length	L
m	Cementation exponent	-
n	Number of pores	-
N_A	Avogadro's number	$1/\text{mol}$
P_h	Normal stress on hydrate exerted by pore walls	M/LT^2
P_l	Pressure in premelted layer	M/LT^2
P_m	Melting pressure in bulk phase	M/LT^2
q_s	Surface charge density	$M^{1/2}/L^{1/2}T$
r	Pore radius	L
r_h	Hydrate radius	L
S	Surface area	L^2
S_h	Hydrate saturation	L^3/L^3
S_s	Specific surface area	L^2/M
S_w	Water saturation	L^3/L^3
T	Temperature	θ
T_0	Reference temperature	θ
T_m	Melting temperature in bulk phase	θ
T_m'	Bulk melting temperature in the presence of salt	θ
V_{EDL}	Total volume of electrical double layers	L^3
$V_{EDL,h}$	Volume of electrical double layer around hydrate	L^3
$V_{EDL,m}$	Volume of electrical double layer around solid matrix	L^3
V_m	Molar volume of water	L^3/mol
V_p	Total pore volume	L^3
V_p'	Pore volume not occupied by hydrate or part of an electrical double layer	L^3
V_s	Volume of solids	L^3
V_T	Total volume	L^3
β_+^f	Cation mobility in bulk fluid	$L^{3/2}/M^{1/2}$
β_-^f	Anion mobility in bulk fluid	$L^{3/2}/M^{1/2}$
ΔH	Latent heat of fusion	L^2/T^2

ε	Relative dielectric permittivity of aqueous phase	-
ε_0	Vacuum dielectric permittivity	L/L
ζ	Zeta potential	$M^{1/2}L^{1/2}/T$
θ	Contact angle	-
g_f	Temperature constant for conductivity	$1/\theta$
κ	Inverse Debye length	$1/L$
λ	Mean free path of water molecules	L
Π	Disjoining pressure	M/LT^2
Π_e	Electrostatic contribution to disjoining pressure	M/LT^2
Π_s	Solvation contribution to disjoining pressure	M/LT^2
Π_{vdW}	van der Waals contribution to disjoining pressure	M/LT^2
ρ_h	Bulk density of hydrate	M/L^3
σ	DC electrical conductivity	$1/T$
σ_{hw}	Hydrate-water interfacial tension	M/T^2
σ_s	Surface conductivity	$1/T$
σ_w	Bulk pore fluid conductivity	$1/T$
φ	Porosity	L^3/L^3
φ'	Porosity not occupied by hydrate or part of an electrical double layer	L^3/L^3
Φ_e	Electrostatic interaction potential	M/T^2
Φ_s	Solvation interaction potential	M/T^2
Φ_{vdW}	van der Waals interaction potential	M/T^2

1043 **Table 1.** Nomenclature